


Cryoablation triggers type I interferon-dependent antitumor immunity and potentiates immunotherapy efficacy in lung cancer

Chuanjia Gu,^{1,2,3} Xue Wang,⁴ Kaiyu Wang,^{4,5} Fangfang Xie,^{1,2,3} Luonan Chen,^{4,5,6,7,8} Hongbin Ji,^{4,5,6,7} Jiayuan Sun ^{1,2,3}

To cite: Gu C, Wang X, Wang K, *et al.* Cryoablation triggers type I interferon-dependent antitumor immunity and potentiates immunotherapy efficacy in lung cancer. *Journal for ImmunoTherapy of Cancer* 2024;**12**:e008386. doi:10.1136/jitc-2023-008386

► Additional supplemental material is published online only. To view, please visit the journal online (<http://dx.doi.org/10.1136/jitc-2023-008386>).

CG, XW, KW and FX contributed equally.

Accepted 11 January 2024



© Author(s) (or their employer(s)) 2024. Re-use permitted under CC BY-NC. No commercial re-use. See rights and permissions. Published by BMJ.

For numbered affiliations see end of article.

Correspondence to

Dr Jiayuan Sun;
xkyjysun@163.com

Hongbin Ji; hbji@sibcb.ac.cn

ABSTRACT

Background Cryoablation is a minimally invasive option for patients with medically inoperable non-small cell lung cancer (NSCLC) and can trigger abscopal immune-regulatory effects. However, it remains unclear how cryoablation affects the host-level immune response in NSCLC. In this study, we investigated the local and systemic immunological effects of cryoablation and the potential of combining cryoablation with programmed cell death protein 1 (PD-1) blockade to boost immunotherapy efficacy in NSCLC.

Methods We first investigated systemic immunological effects induced by cryoablation in patients with early-stage NSCLC. Subsequently, we explored cryoablation-induced antitumor immunity and the underlying biological mechanisms using KP (*Kras*^{G12D/+}, *Tp53*^{-/-}) mutant lung cancer cell allograft mouse models. Moreover, the synergistic efficacy of cryoablation and PD-1 blockade was explored in both mouse models and patients with unresectable NSCLC.

Results We found that cryoablation significantly increased circulating CD8⁺ T cell subpopulations and proinflammatory cytokines in patients with early-stage NSCLC. In lung cancer cell allograft mouse models, we demonstrated that cryoablation resulted in abscopal growth inhibition of contralateral, non-ablated tumors. Integrated analysis of bulk, single-cell RNA and T cell receptor (TCR) sequencing data revealed that cryoablation reprogrammed the intratumoral immune microenvironment and increased CD8⁺ T cell infiltration with higher effector signature, interferon (IFN) response, and cytolytic activity. Mechanistically, cryoablation promoted antitumor effect through the STING-dependent type I IFN signaling pathway, and type I IFN signaling blockade attenuated this antitumor effect. We also found that the combination of PD-1 blockade with cryoablation further inhibited tumor growth compared with either treatment alone in an allograft mouse model. Moreover, the combination therapy induced notable tumor suppression and CD8⁺ T cell infiltration in patients with unresectable NSCLC.

Conclusions Our results provide mechanistic insights into how cryoablation triggers the antitumor immune effect in lung cancer, thereby potentiating programmed cell death ligand 1 (PD-L1)/PD-1 blockade efficacy in the clinical treatment of NSCLC.

WHAT IS ALREADY KNOWN ON THIS TOPIC

⇒ Local tumor cryoablation is an effective non-surgical treatment for local tumor control and can enhance immunotherapy efficacy in some preclinical cancer models.

WHAT THIS STUDY ADDS

⇒ Our work reveals a type I interferon-dependent antitumor immune response elicited by cryoablation and further demonstrates the enhanced synergistic efficacy of cryoablation in combination with anti-programmed cell death protein 1 (PD-1)-based immunotherapy in patients with non-small cell lung cancer (NSCLC).

HOW THIS STUDY MIGHT AFFECT RESEARCH, PRACTICE OR POLICY

⇒ Our data provide mechanistic insights into how cryoablation boosts antitumor immunity and initial clinical evidence supporting the experimental strategy of combining cryoablation with anti-PD-1 therapy in NSCLC to enhance immunotherapy efficacy.

INTRODUCTION

Lung cancer remains the leading cause of cancer-related death worldwide.¹ Local tumor cryoablation has been increasingly applied in clinic as a minimally invasive treatment option for non-small cell lung cancer (NSCLC),²⁻⁴ providing an alternative local therapy for lung tumors to surgical resection and radiation therapy.^{5,6} Among these methods, cryoablation may be better tolerated and provide better preservation of the lung tissue.⁷ During cryoablation, the rapid expansion of pressurized nitrogen or argon gas cools the cryoprobe to less than -140°C, enabling the destruction of target tissues. Importantly, cryoablated tissues left in situ serve as a source of tumor-specific antigens capable of eliciting an immune response against sublethally damaged or even untreated tissues, which is similar to a

vaccination, potentially yielding an abscopal effect.⁸ Early studies since the late 1970s have recognized this immunological effect of cryoablation in several case reports, in which untreated metastatic lesions exhibited regression.⁹ Although preclinical animal models have shown that cryoablation can induce immunogenic changes across several malignancies,^{10,11} evidence remains limited in NSCLC. The underlying mechanisms of cryoablation-induced antitumor immune responses in primary and distant tumors of NSCLC remain obscure.

Recent years have witnessed the emergence of immune checkpoint inhibitors (ICIs) as systemic treatments for NSCLC, showing remarkable efficacy.^{12,13} However, unresponsiveness to cancer immunotherapy has been noted in some patients, which potentially is attributed to inadequate tumor infiltration of tumor-specific T cells in NSCLC. Considering that cryoablation may have the capacity to modify the immune landscape of patients with malignancies, combining ICIs-based immunotherapy and cryoablation to boost immunotherapy efficacy may be promising and deserves further investigations.

Therefore, we aimed to investigate the local and systemic immunological effects of cryoablation and its possible underlying mechanisms. We first found that cryoablation modified host-level immune responses in early-stage NSCLC. Subsequently, we explored cryoablation-induced antitumor immunity using lung cancer cell allograft mouse models. Our data revealed that cryoablation reprogrammed the intratumoral immune microenvironment and promoted type I interferon (IFN)-dependent antitumor effect. Moreover, we demonstrated that combined therapy with cryoablation and programmed cell death protein 1 (PD-1) blockade exhibited great efficacy and enhanced immune infiltration in both mouse models and patients with NSCLC. Taken together, our study sheds light on the cryoablation-induced abscopal effect and demonstrates enhanced synergistic efficacy with anti-PD-1 therapy, suggesting the promising potential of a combination strategy involving cryoablation and PD-1 blockade immunotherapy in patients with NSCLC in clinical practice.

MATERIALS AND METHODS

Patients and specimens

Peripheral blood and biopsy samples were obtained from patients with NSCLC at Shanghai Chest Hospital, Shanghai Jiao Tong University School of Medicine. The enrolled patients were ineligible for surgery or refused surgery. Peripheral blood samples (n=6) were collected from patients with early-stage NSCLC before cryoablation and at various time points (1, 3, 7, and 14 days) post-cryoablation. We isolated peripheral blood mononuclear cells using Ficoll-Paque density gradient media (Cytiva) to assess the changes of lymphocyte populations using flow cytometry. Plasma was extracted after centrifugation for examination of key inflammation biomarkers using Bio-Plex Pro Human Inflammation Panel 1, 37-Plex Kit

(Bio-Rad). Biopsy specimens (n=3) were obtained from patients treated with cryoablation combined with anti-PD-1 immunotherapy to evaluate the changes within the tumor microenvironment (TME) before and after the combined therapy.

Written informed consent about the procedure and clinical trial was obtained from all the participants.

Cell culture

KP,¹⁴ KL,¹⁵ and Lewis lung cancer (LLC) cells were used in this study. KP and LLC cells were cultured in a 37°C and 5% CO₂ incubator, using Dulbecco's modified Eagle's medium (DMEM) supplemented with 10% fetal bovine serum (FBS) and 100 units/mL penicillin plus streptomycin. KL cells were cultured under the same conditions, using RPMI 1640 medium supplemented with 10% FBS and 100 units/mL penicillin plus streptomycin. All cell lines were authenticated and free of *Mycoplasma* contamination.

Mouse lung cancer allograft assay and treatments

All mice were purchased from Zhejiang Vital River Laboratory Animal Technology (Zhejiang, China) and housed in a pathogen-free environment at Shanghai Chest Hospital. For detailed methods of mouse lung cancer allograft assay and treatment, refer to online supplemental material.

Total RNA extraction and quantitative real-time PCR

Total RNA was extracted from tumor tissues using TRIzol Reagent (Invitrogen). Subsequently, cDNA was synthesized using the RevertAid First Strand cDNA Synthesis Kit (Thermo Scientific). Quantitative real-time (qRT)-PCR was performed using the FastStart Universal SYBR Green Master (Rox) (Roche). The mouse primers used are listed in online supplemental table S1. All the primers were purchased from Tsingke and Sangon Biotech.

Bulk RNA sequencing and data analysis

Total RNA was obtained from contralateral tumor tissues harvested at day 7 postcryoablation from the cryoablation (CA) and non-cryoablation (non-CA) groups (n=3 per group). RNA sequencing was then performed using Illumina NovaSeq 6000 (150 bp paired-end reads). For detailed methods of data analysis for bulk RNA sequencing, refer to online supplemental material.

Flow cytometric analysis

Freshly harvested tumors were dissociated to generate single-cell suspension. Subsequently, immune cells were enriched and stained with indicated fluorochrome-conjugated antibodies in FACS buffer (phosphate buffered saline (PBS)+2% FBS+1 mM EDTA). Flow cytometry was performed using BD FACS Fortessa. Data were analyzed with FlowJo V.10.8.1 software. For detailed methods of flow cytometric analysis, refer to online supplemental material.

Single-cell RNA and V(D)J sequencing

Intratumoral CD45⁺ immune cells were isolated at day 7 and CD45⁺CD3⁺ T cells were isolated at days 7 and 14 after cryoablation using BD FACSAria III. The single-cell pellet was then resuspended in PBS without calcium and magnesium ions to reach a density of ≤ 1000 cells/ μ L. Single-cell 3' RNA sequencing libraries for CD45⁺ tumor-infiltrating lymphocytes (TILs) were constructed according to the protocols of the Chromium Single Cell 3' Library Kit (10x Genomics) on the Illumina platform. For CD45⁺CD3⁺ TILs, the single-cell suspension was converted to uniquely barcoded RNA and T cell receptor (TCR) libraries by using the Chromium Single Cell 5' Library Kit, Gel Bead and Multiplex Kit, and Chromium Single Cell V(D)J Enrichment Kit following the manufacturer's instructions. Sequencing was performed on the Illumina NovaSeq 150PE platform by Berry Genomics (Beijing, China). For detailed methods of data analysis for single-cell sequencing, refer to online supplemental material.

Multiplex immunoassay

The mouse tumor tissues were homogenized in PBS, and the supernatants were collected. The protein levels of IFN- α and IFN- β were then detected using LEGENDplex Mouse Type 1/2 Interferon Panel (Biolegend) according to the manufacturer's instructions. For detailed methods of multiplex immunoassay, refer to online supplemental material.

Western blot analysis

Protein expression was analyzed by western blot. The bands were visualized by chemiluminescence using Amersham Imager 6000. Gray values of each band were calculated using ImageJ V.1.53 software, and the band intensity of the target protein was normalized by the band intensity of β -actin to reduce the influence of intersample variation. For detailed methods, refer to online supplemental material.

Multiplex immunofluorescence staining

Human biopsies were fixed in 10% formalin, embedded in paraffin, and sectioned at 5 μ m thickness. Multiplex immunofluorescence staining was then performed using Opal 4-Color Manual IHC Kit (Akoya) following the manufacturer's instructions with indicated antibodies (online supplemental table S2) and 4',6-diamidino-2-phenylindole (DAPI). Multispectral immunofluorescent images of stained slides were acquired using Leica TCS SP8 STED.

Statistics

All statistical analyses were performed using SPSS V.25.0 and GraphPad Prism V.8.0. P value ≤ 0.05 was considered to be of significant difference. Data are expressed as mean \pm SEM. For detailed methods of statistics, refer to online supplemental material.

RESULTS

Cryoablation is clinically effective for local control of NSCLC and alters host-level immune profiles

At our center, cryoablation has demonstrated excellent local control in patients with medically inoperable early-stage NSCLC (figure 1A). To explore the effects of cryoablation on the systemic antitumor immune response, we analyzed the changes of immune cell subsets in peripheral blood samples by flow cytometry. The gating strategy is illustrated in online supplemental figure S1A. We observed a significant increase in the proportion of CD8⁺ T cells after cryoablation, whereas the proportion of CD4⁺ T cells remained unchanged (figure 1B–D). We also noticed that there were no significant changes in the frequencies of naive CD8⁺ T cells (CD45RA⁺CCR7⁺), central memory CD8⁺ T cells (CD45RA⁻CCR7⁺), effector CD8⁺ T cells (CD45RA⁺CCR7⁻), or effector memory CD8⁺ T cells (CD45RA⁻CCR7⁻) between pretreatment and post-treatment (online supplemental figure S1B). Moreover, four out of six patients exhibited a reduction in the proportion of Foxp3⁺ regulatory T cells (Tregs), and five out of six patients exhibited an increased ratio of CD8⁺ T cells to Tregs after cryoablation (online supplemental figure S1C,D). We also found that a broad panel of inflammatory biomarkers, including interleukin (IL)-2, IL-11, IL-29, and matrix metalloproteinase 3 (MMP-3), were significantly increased after cryoablation (figure 1E and online supplemental figure S1E–H). Collectively, our results demonstrate the promising clinical benefits of cryoablation, highlighting its potential to induce systemic immune response beyond the ablation zone in patients with NSCLC.

Cryoablation induces an antitumor abscopal effect on the non-ablated tumors

To explore the immune response induced by cryoablation, we employed a bilateral lung tumor model in which a KP genetically engineered mouse model (GEMM)-derived primary cell line was inoculated subcutaneously into the bilateral flanks of C57BL/6 mice (figure 2A). First, we sought to determine whether cryoprobe insertion or damage caused by cryoablation of normal tissue leads to abscopal tumor growth inhibition. We did a preliminary experiment and designed four groups, namely no treatment (non-CA), cryoprobe insertion without cryoablation (sham treatment), cryoablation of normal skin tissue (sham CA), and cryoablation of tumor tissue (CA; online supplemental figure S2A). We found that there was no significant difference in the growth of contralateral tumors between non-CA, sham treatment, and sham CA groups (online supplemental figure S2B). Therefore, we used non-CA as the control group in our follow-up study. Under the condition of two freeze–thaw cycles with liquid nitrogen, the tumors on the lateral side of the cryoablation were completely ablated (online supplemental figure S2C) and the growth of the contralateral tumors slowed down (figure 2B). At day 14 after cryoablation, the tumor weight was significantly reduced in the CA group compared with that in the non-CA group (figure 2C). This finding was also confirmed in two other transplantable models of lung cancer cell lines, KL cells, a *Kras*^{G12D/+} *Lkb1*^{-/-} GEMM-derived

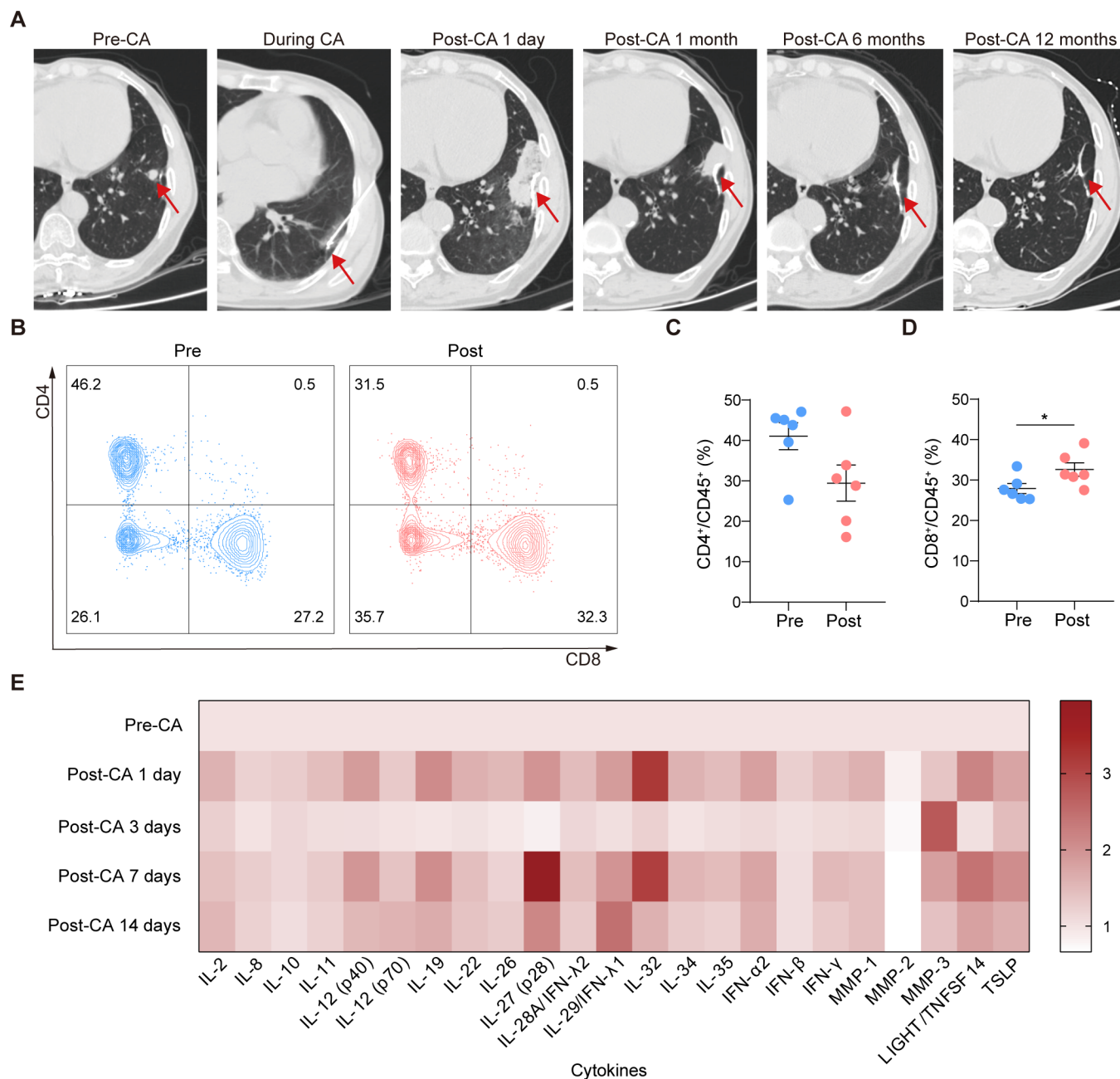


Figure 1 Cryoablation modulates the host-level immune response in human NSCLC. (A) Representative CT scans of a patient with early-stage NSCLC treated with cryoablation. The red arrows indicate the target lesions. (B–D) Flow cytometric analysis of CD4⁺ and CD8⁺ T cells in peripheral blood samples collected before cryoablation and at day 1 after cryoablation from patients with early-stage NSCLC (n=6). (E) Cytokine secretion displayed as heatmap in the peripheral blood samples collected before cryoablation and at days 1, 3, 7, and 14 after cryoablation from patients with early-stage NSCLC (n=6). The results are shown as mean \pm SEM, and the statistical significance of differences between groups was determined by unpaired Student's t-test (*p<0.05). CA, cryoablation; NSCLC, non-small cell lung cancer; IL, interleukin; IFN, interferon; MMP, matrix metalloproteinase; TSLP, thymic stromal lymphopoietin; LIGHT, lymphotoxin-related inducible ligand that competes for glycoprotein D binding to herpesvirus entry mediator on T cells; TNFSF, tumor necrosis factor superfamily.

primary cell line, and LLC cells (online supplemental figure S2D). Collectively, these results demonstrate that the destruction on tumor tissues caused by cryoablation promotes abscopal growth inhibition of contralateral, non-ablated tumors in lung cancer cell allograft mouse models.

Cryoablation triggers an inflammatory process and activates antitumor immune response

To further elucidate the underlying mechanism of the abscopal effect induced by cryoablation, we performed bulk RNA sequencing using contralateral, non-ablated KP tumors at day 7 after cryoablation. Hallmark pathway analysis revealed that cryoablation induced significant transcriptional changes in distant tumors, notably a

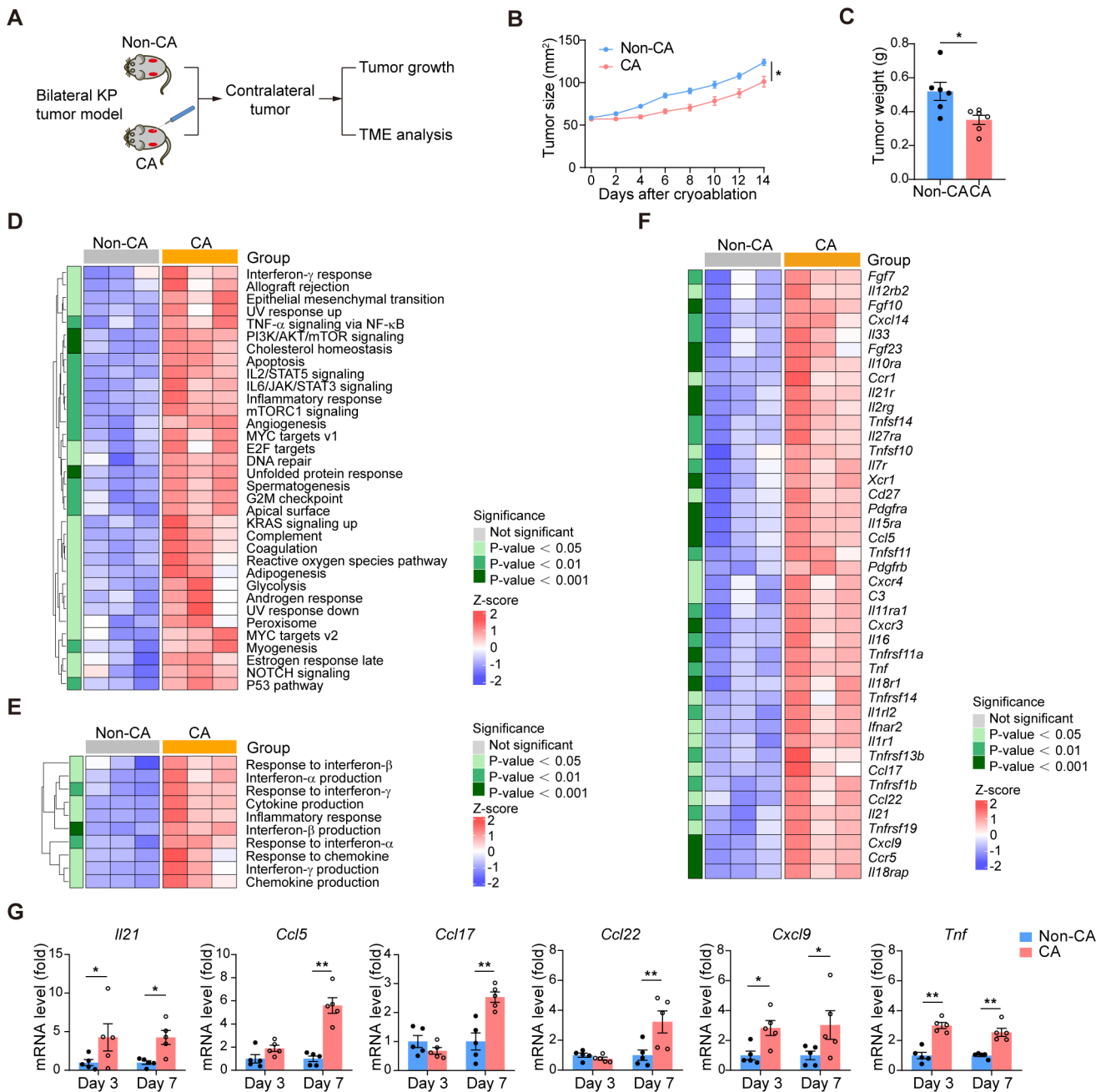


Figure 2 Cryoablation induces inhibition of contralateral tumor growth and promotes inflammatory responses in KP tumor-bearing mice. (A) Schematic illustration of the experimental design. (B and C) Mean tumor growth (B) and tumor weight (at day 14; C) of contralateral KP tumors in the non-CA and CA groups ($n=6$ per group). (D) Heatmap of the hallmark pathways in contralateral KP tumors from the non-CA and CA groups at day 7 after cryoablation ($n=3$ per group). (E) Heatmap of IFN, cytokines, and chemokines-related pathways ($n=3$ per group). (F) Heatmap of differential cytokines and chemokines ($n=3$ per group). (G) mRNA levels of intratumoral cytokines and chemokines at days 3 and 7 after cryoablation ($n=5$ per group). The results are shown as mean \pm SEM, and the statistical significance of differences between groups was determined by unpaired Student's t-test (* $p<0.05$, ** $p<0.01$). CA, cryoablation; IFN, interferon; TME, tumor microenvironment.

significant upregulation of signaling pathways related to inflammatory responses, including IFN- γ response, IL2/STAT5 signaling, IL6/JAK/STAT3 signaling, etc (figure 2D). Subsequently, we screened immune-related pathways and identified several major pathways that were highly enriched in the CA group, including the production of IFN- α , IFN- β , and IFN- γ , as well as their immune responsive pathways (figure 2E). We also found increased

levels of various proinflammatory cytokines and chemokines (figure 2E,F), including IL-21, C-C motif chemokine ligand (CCL) 5, CCL17, CCL22, C-X-C motif chemokine ligand (CXCL) 9, and tumor necrosis factor (TNF), which was further confirmed by qRT-PCR (figure 2G).

Furthermore, we analyzed the infiltrating immune cells in contralateral tumors. The gating strategy is illustrated in online supplemental figure S3A. The percentage of

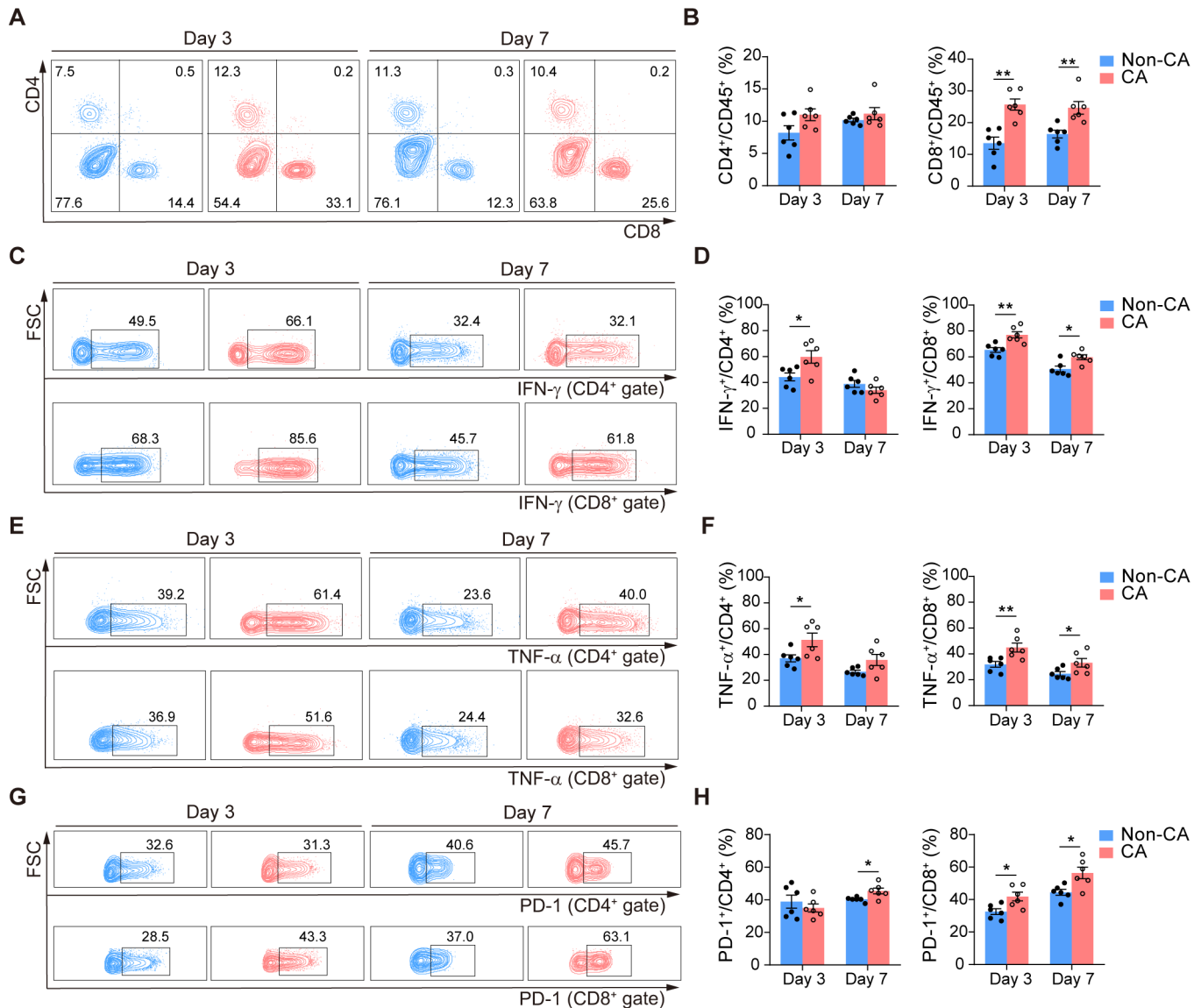


Figure 3 Cryoablation induces extensive intratumoral immune cell infiltration with enhanced cytotoxic capacities and exhaustion features in contralateral KP tumors. (A and B) Representative flow cytometric plots (A) and the percentage (B) of CD4⁺ and CD8⁺ TILs in contralateral KP tumors from the non-CA and CA groups at days 3 and 7 after cryoablation (n=6 per group). (C and D) Representative flow cytometric plots (C) and the percentage (D) of IFN-γ⁺CD4⁺ and IFN-γ⁺CD8⁺ TILs (n=6 per group). (E and F) Representative flow cytometric plots (E) and the percentage (F) of TNF-α⁺CD4⁺ and TNF-α⁺CD8⁺ TILs (n=6 per group). (G and H) Representative flow cytometric plots (G) and the percentage (H) of PD-1⁺CD4⁺ and PD-1⁺CD8⁺ TILs (n=6 per group). The results are shown as mean±SEM, and the statistical significance of differences between groups was determined by an unpaired Student's t-test (*p<0.05, **p<0.01). CA, cryoablation; FSC, forward scatter; IFN, interferon; PD-1, programmed cell death protein 1; TILs, tumor-infiltrating lymphocytes; TNF, tumor necrosis factor.

NK1.1⁺ natural killer (NK) cells exhibited a significant increase at day 3 after cryoablation (online supplemental figure S3B,C). More importantly, we noticed that T cell infiltration was characterized by an increased frequency of CD8⁺ T cells at days 3 and 7 (figure 3A,B). The percentage of Tregs remained comparable with that in the non-CA group at days 3 and 7 (online supplemental figure S3D,E). However, the CD8⁺ T cell to Treg ratio was significantly increased at day 3 after cryoablation (online supplemental figure S3F).

Next, we analyzed the effector function of TILs. The production of IFN-γ and TNF-α by CD4⁺ and CD8⁺ T cells

was significantly increased at day 3, and the percentage of IFN-γ⁺CD8⁺ and TNF-α⁺CD8⁺ TILs remained higher than that in untreated mice at day 7 (figure 3C–F). The production of granzyme B on CD8⁺ T cells was also significantly increased at day 3 (online supplemental figure S3G,H). Furthermore, we observed that the expression of PD-1 was increased on CD8⁺ TILs at day 3. A further increase of PD-1 expression on both CD4⁺ and CD8⁺ TILs was observed at day 7 (figure 3G,H). These data indicate that cryoablation provoked a strong inflammatory response in the distant tumors and remodeled the composition and functional state of TILs.

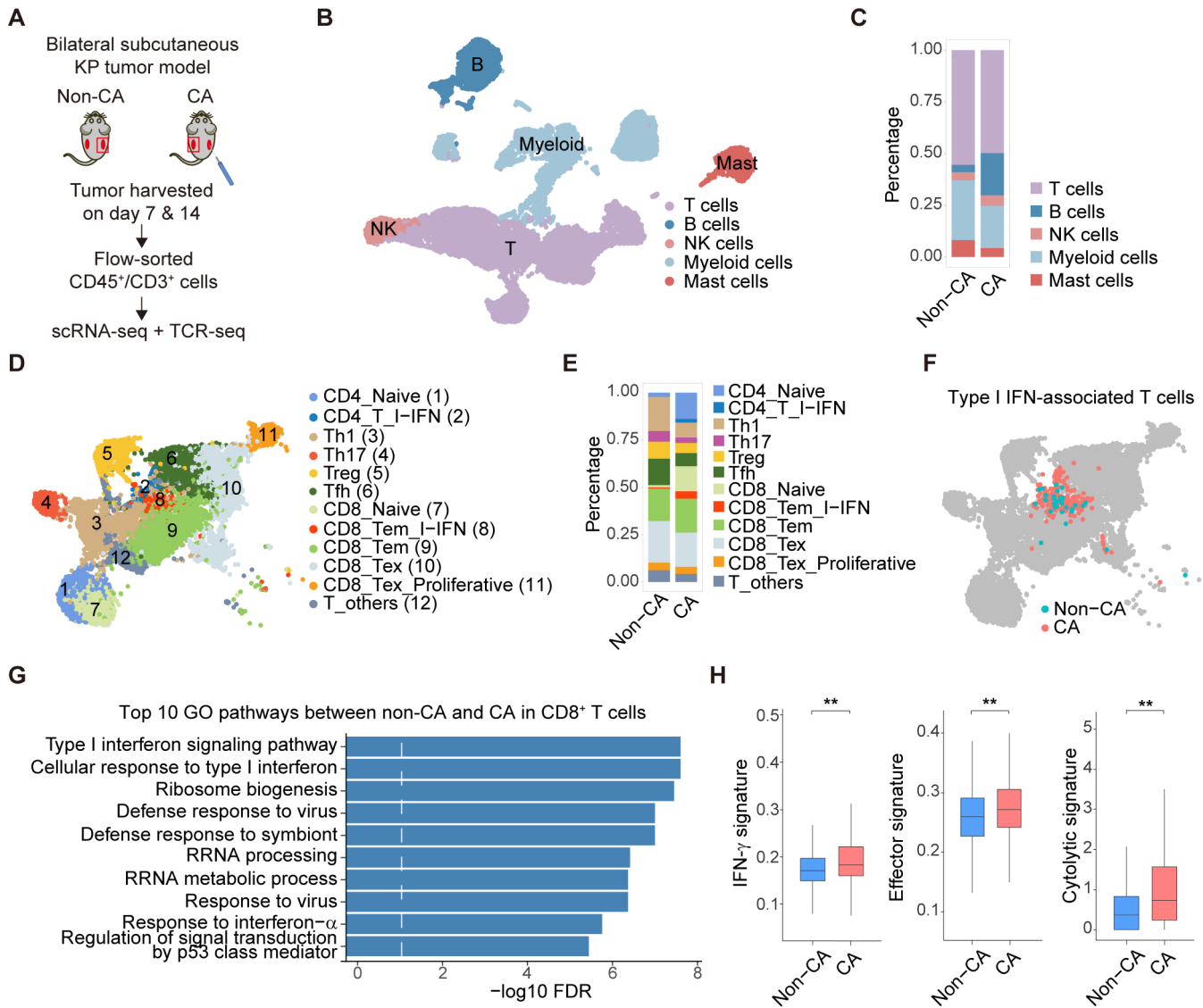


Figure 4 Cryoablation reprograms intratumoral immune cells and promotes activation features in CD8⁺ TILs through scRNA-seq. (A) Schematic diagram illustrating the experimental strategy for scRNA-seq and scTCR-seq. (B) UMAP embeddings of scRNA-seq profiles of CD45⁺ immune cells in contralateral KP tumors at day 7 after cryoablation. (C) Bar plot demonstrating the percentages of cell subpopulations, related to the UMAP plot in (B). (D) UMAP embeddings of scRNA-seq profiles of CD3⁺CD45⁺ T cells in contralateral KP tumors at day 7 after cryoablation. (E) Bar plot demonstrating the percentages of T cell subpopulations, related to the UMAP plot in (D). (F) Type I IFN-associated T cells from the non-CA and CA groups. (G) GO pathway enrichment analysis of CD8⁺ TILs based on the differentially expressed genes between the non-CA and CA groups. (H) Box plot indicating IFN- γ response, effector, and cytolytic signatures of CD8⁺ TILs. The statistical significance of differences between groups was determined by the non-parametric Wilcoxon rank-sum test with Bonferroni correction (**p < 0.01). CA, cryoablation; FDR, false discovery rate; GO, Gene Ontology; NK, natural killer; scRNA-seq, single-cell RNA sequencing; scTCR-seq, single-cell TCR sequencing; Tem, effector memory T cells; Tex, exhausted T cells; Th, T helper; TILs, tumor-infiltrating lymphocytes; Tregs, regulatory T cells; UMAP, uniform manifold approximation and projection.

Cryoablation reprograms intratumoral immune cells and promotes type I IFN pathway in T cells by scRNA-seq

To further investigate the impact of cryoablation on the TME, we performed single-cell RNA sequencing (scRNA-seq) on CD45⁺ immune cells and single-cell TCR sequencing (scTCR-seq) on CD45⁺CD3⁺ T cells isolated from contralateral, non-ablated tumors in KP tumor-bearing mice (figure 4A). After data preprocessing and quality control, we acquired a total of 17670 CD45⁺ immune cells with high-quality single-cell transcriptomes

(8649 cells from the non-CA group and 9021 cells from the CA group) and identified five clusters, including T, B, NK, mast, and myeloid cells, according to the expression patterns of the marker genes (figure 4B and online supplemental figure S4A). The relative abundance showed that T and myeloid cells were the most predominant cell types in the KP microenvironment (figure 4C). Otherwise, we observed a marked increase in the proportion of B cells within the tumors from the CA group. Hence, we performed Gene Ontology (GO) pathway enrichment

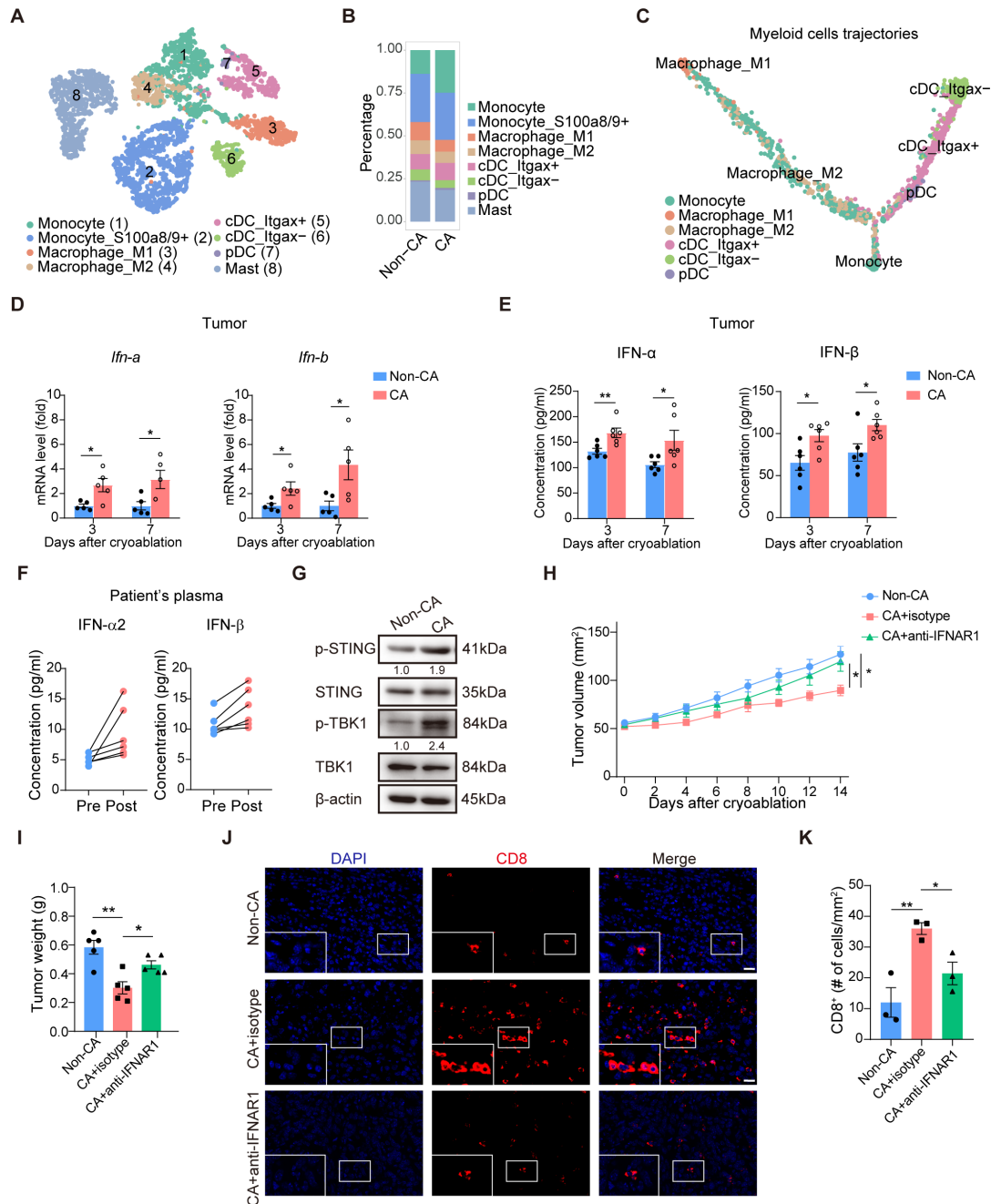


Figure 5 Cryoablation reprograms tumor-infiltrating myeloid cells and promotes type I IFN-induced immune responses in a STING-dependent manner. (A) UMAP embeddings of scRNA-seq profiles of myeloid cells in contralateral KP tumors at day 7 after cryoablation. (B) Bar plot demonstrating the percentages of cell subpopulations, related to the UMAP plot in (A). (C) The developmental trajectory of myeloid cells. (D) mRNA level of type I IFN in contralateral KP tumors (n=5 per group). (E) Type I IFN protein concentration in contralateral KP tumor tissue homogenate (n=6 per group). (F) The level of type I IFN secretion in the peripheral blood samples collected before and at day 1 after cryoablation from patients with early-stage NSCLC (n=6). (G) Immunoblot analysis of p-STING, STING, p-TBK1, and TBK1 in contralateral KP tumors from the non-CA and CA groups. The numbers indicate the relative densities of indicated protein bands normalized to β -actin. (H and I) Mean tumor growth (H) and tumor weight (I) of contralateral KP tumors after the treatment of cryoablation combined with an anti-IFNAR1 blocking antibody or an isotype control monoclonal antibody (n=5 per group). (J and K) Immunofluorescence staining (J) and count (K) of tumor-infiltrating CD8⁺ T cells in contralateral KP tumors after the treatment of cryoablation combined with an anti-IFNAR1 blocking antibody or an isotype control monoclonal antibody (n=3 per group). Scale bar: 20 μ m. The statistical significance of differences between two groups was determined by unpaired Student's t-test and the statistical significance of differences among multiple groups was determined by one-way analysis of variance (* p <0.05, ** p <0.01). CA, cryoablation; cDC, conventional dendritic cell; DAPI, 4', 6-diamidino-2-phenylindole; IFN, interferon; IFNAR1, interferon alpha/beta receptor subunit 1; NSCLC, non-small cell lung cancer; pDC, plasmacytoid dendritic cell; p-STING, phosphorylated stimulator of interferon genes; p-TBK1, phosphorylated TANK binding kinase 1; scRNA-seq, single-cell RNA sequencing; STING, stimulator of interferon genes; TBK1, TANK binding kinase 1; UMAP, uniform manifold approximation and projection.

analysis specifically for B cells based on the differentially expressed genes. The analysis revealed a significant enhancement in antigen processing and presentation via major histocompatibility complex (MHC) class II, suggesting augmented MHC class II presentation of exogenous antigen and peptides to CD4⁺ T cells for its activation (online supplemental figure S4B).

We then comprehensively characterized the heterogeneous subpopulations within the infiltrating T cells and identified 12 major clusters (figure 4D and online supplemental figure S4C,D). More importantly, we identified a subpopulation with high expression of type I IFN-stimulated genes (ISGs) in CD4⁺ and CD8⁺ T cells (online supplemental figure S4E), which was specifically enriched in the CA group (figure 4E,F). Meanwhile, we used ProjecTIL to project all T cells onto a reference T cell atlas following the methodology proposed by Andreatta *et al.*¹⁶ (online supplemental figure S4F,G), confirming the clustering accuracy of T cells.

Subsequently, GO pathway analysis also revealed upregulation of type I IFN-associated pathways in all T cells, CD8⁺ T cells, and effector memory CD8⁺ T cells (Tem) from the CA group (figure 4G and online supplemental figure S5A,B), which suggests that T cells in the CA group were significantly influenced by type I IFN induced by cryoablation. To further explore the role of type I IFN-stimulated clusters in the lineage structure of CD8⁺ T cells, we performed the pseudotime developmental trajectory analysis on CD8⁺ T cells (online supplemental S5C–E) and observed a continuous differentiation trajectory in the non-CA group, starting from naïve T cells toward Tem cells and ending with exhausted T cells (Tex) and proliferative Tex cells (online supplemental figure S5D). In contrast, pseudotime analysis of CD8⁺ T cells in the CA group exhibited a transitional process from naïve T cells and Tem cells to proliferative Tex cells through an intermediate type I IFN-stimulated Tem (CD8_Tem_I-IFN) state (online supplemental figure S5E). These results suggest that type I IFN-stimulated CD8⁺ Tem cells, which were specifically amplified in the CA group, might serve as a crucial transitional state during CD8⁺ T cell differentiation. Moreover, the pseudotime analysis also demonstrated that exhaustion represented the terminal stage during CD8⁺ T cell development, and the combination of cryoablation to reactivate Tex could potentially emerge as a potent therapy to prolong antitumor immunity.

Cryoablation expands CD8⁺ TILs with effector and exhaustion features

To further explore the functional state of T cells, we performed gene set enrichment analysis for functional signatures and found enhanced IFN- γ response scores, effector T cell gene signatures, and cytolytic activity in CD8⁺ T cells after cryoablation (figure 4H). Moreover, the functional scores calculated using Gong *et al.*'s model¹⁷ demonstrated a significant decrease in naïve scores and an increase in exhaustion scores in the CA group (online supplemental figure S5F). These results highlight the

enhancement of cytotoxicity accompanied with exhaustion features in CD8⁺ TILs.

We next isolated CD3⁺ T cells at days 7 and 14 following cryoablation and systematically analyzed the TCR identity on individual T cells based on the coupled V(D)J profiling to characterize the clonal diversity of infiltrated T cells after cryoablation. We used paired scTCR and scRNA profiling to integrate clonotype profiling with T cell phenotypes so as to infer phenotypic activities. Among all the subpopulations of T cells, CD8⁺ Tem cells displayed increased clonal expansion in the CA group at day 7, followed by a marked decrease at day 14, ultimately resembling the pattern observed in untreated mice (online supplemental figure S5G). This suggests that CD8⁺ Tem cells within the KP TME may indeed be reinvigorated to elicit clonotypic changes in response to cryoablation at an early stage.

To elucidate the reason for the increased fraction of naïve T cells in the CA group, we further applied clonotype neighbor graph analysis¹⁸ to correlate gene expression (GEX) profiles and TCR sequence using bicolored discs, with the left and right halves corresponding to GEX and TCR cluster assignments, respectively. The results indicated that expanded naïve T cells share similar TCR clusters with effector T cells (online supplemental figure S6), suggesting that these naïve T cells tend to undergo initial activation in terms of TCR phenotype, which is not yet manifested in the GEX profiles. Therefore, we hypothesized that the expansion of these initially activated T cells may act as a reservoir for subsequent rapid transformation into functional T cells.

Cryoablation reprograms myeloid cells and promotes antitumor effect through the STING-dependent type I IFN pathway

With 5108 myeloid cells clustered into eight subpopulations (figure 5A and online supplemental figure S7A), we observed alterations in the proportions of myeloid cells, especially higher frequencies of monocytes in the CA group (figure 5B). The developmental trajectory of myeloid cells validated the capability of monocytes to differentiate into macrophages and dendritic cells (DCs) (figure 5C). Furthermore, we performed GO analysis and found the enrichment of responses to type I IFN (online supplemental figure S7B). Hence, we hypothesized that type I IFN-related pathways participate in the antitumor effect of cryoablation.

To investigate this, we first examined type I IFN production in contralateral tumors of the non-CA and CA groups and found that the mRNA and protein levels of IFN- α and IFN- β were significantly increased at days 3 and 7 in the CA group (figure 5D,E). Moreover, we observed an elevated trend in the concentrations of IFN- α and IFN- β in the plasma of patients with NSCLC who underwent cryoablation, especially at day 1 after cryoablation (figure 5F and online supplemental figure S11,J). Recent studies have indicated that the cyclic GMP-AMP synthase-stimulator of interferon genes (cGAS–STING) pathway facilitates the

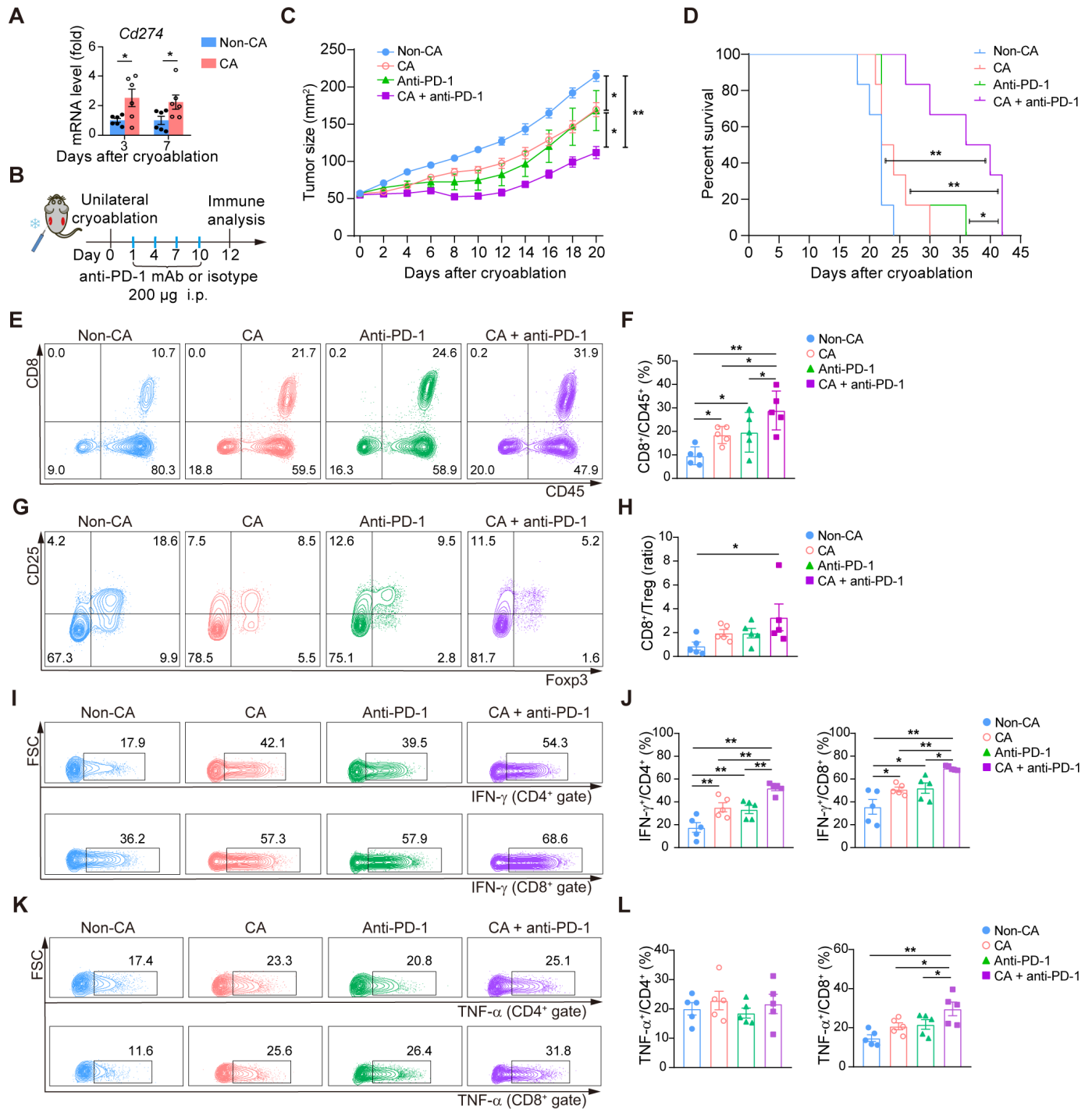


Figure 6 Cryoablation combined with anti-PD-1 synergistically enhanced antitumor immunity in KP tumor-bearing mice. (A) mRNA level of PD-L1 expression in contralateral tumors at days 3 and 7 after cryoablation. (B) Schematic diagram of the combined treatment. (C and D) Mean tumor growth of the contralateral tumors (C) and survival curves of KP tumor-bearing mice (D) after the combined treatment of cryoablation with an anti-PD-1 or isotype control monoclonal antibody. (E and F) Representative flow cytometric plots (E) and the percentage (F) of CD8⁺ TILs at day 12 after the combined therapy. (G) Representative flow cytometric plots showing CD25⁺Foxp3⁺ Tregs at day 12 after the combined therapy. (H) The ratio of CD8⁺ TILs to Tregs (n=5 per group). (I and J) Representative flow cytometric plots (I) and the percentage (J) of IFN-γ⁺CD4⁺ and IFN-γ⁺CD8⁺ TILs in the non-CA and CA groups (n=5 per group). (K and L) Representative flow cytometric plots (K) and the percentage (L) of TNF-α⁺CD4⁺ and TNF-α⁺CD8⁺ TILs in the non-CA and CA groups (n=5 per group). The statistical significance of differences between two groups was determined by unpaired Student's t-test and the statistical significance of differences among multiple groups was determined by one-way analysis of variance. Survival curves were analyzed by log-rank (Mantel-Cox) test (*p<0.05, **p<0.01). CA, cryoablation; FCS, forward scatter; IFN, interferon; mAb, monoclonal antibody; PD-1, programmed cell death protein 1; PD-L1, programmed cell death ligand 1; TILs, tumor-infiltrating lymphocytes; TNF, tumor necrosis factor; Tregs, regulatory T cells.

Table 1 Baseline characteristics of patients with NSCLC treated with cryoablation combined with PD-1 blockade

Case	Gender	Pathology	Stage	PD-L1 expression (%)	Duration of response (months)
1	Male	LUSC	IIb	60	12
2	Male	LUAD	IIa	50	44*
3	Male	LUAD	IIIa	50	5
4	Male	LUSC	IVb	40	9*
5	Male	LUAD	IIIa	90	14*
6	Male	LUAD	IVa	100	9*

*Patient is still being followed up and has not yet reached the study endpoint.

LUAD, lung adenocarcinoma; LUSC, lung squamous cell carcinoma; NSCLC, non-small cell lung cancer; PD-1, programmed cell death protein 1; PD-L1, programmed cell death ligand 1.

innate recognition of irradiated tumor cells, leading to enhanced antitumor immunity through the generation of type I IFNs.¹⁹ Hence, we proceeded to analyze the activation of STING signaling. The results showed that STING and TANK binding kinase 1 (TBK1) phosphorylation were upregulated in the CA group (figure 5G), suggesting that cryoablation might enhance STING-dependent type I IFN responses. We further analyzed the activity of type I IFN production in various tumor-infiltrating immune cell types with scRNA-seq data to find out which cells produce type I IFNs in the TME. We found that the activity of type I IFN production was significantly elevated in monocytes and DCs (online supplemental figure S7C,D).

To further validate that type I IFN plays an important role in cryoablation-induced antitumor immunity, we treated KP tumor-bearing mice with an anti-interferon alpha/beta receptor subunit 1 (IFNAR1) blocking antibody. The results showed that the inhibition of tumor growth induced by cryoablation was almost eliminated by IFNAR1 blockade (figure 5H,I). Additionally, the recruitment of CD8⁺ T cells (figure 5J,K) as well as the expression of proinflammatory cytokines and chemokines (online supplemental figure S7E) were also compromised in the absence of type I IFN signaling. Collectively, these data indicate that cryoablation may modulate antitumor immunity through the STING-dependent type I IFN pathway.

Cryoablation combined with anti-PD-1 synergistically enhances antitumor immunity in KP allograft mouse model

Our data demonstrated increased immune cell infiltration and upregulated PD-1 expression in T cells following cryoablation. Accordingly, qRT-PCR confirmed the upregulation of PD-L1 expression in the contralateral tumor tissues (figure 6A). Given that cryoablation could enhance the PD-1/PD-L1 axis, we postulated that subsequent anti-PD-1 therapy would further improve antitumor immunity.

To test this hypothesis, we treated subcutaneous KP mice with cryoablation plus anti-PD-1 (CA+anti-PD-1 group), cryoablation plus an isotype control antibody (CA group), anti-PD-1 alone (anti-PD-1 group), or left them untreated (non-CA group). We observed tumor growth and mouse survival and collected contralateral tumor tissues for immune analysis at day 12 (figure 6B). The results showed that the CA+anti-PD-1 group demonstrated more pronounced inhibition of tumor growth and prolonged survival than the other groups (figure 6C and D).

We further analyzed the tumor-infiltrating immune cells and found that the CA+anti-PD-1 group exhibited a notably higher frequency of infiltrating CD8⁺ cells than the other groups at day 12. The CA and anti-PD-1 groups also demonstrated a higher percentage of CD8⁺ T cells than the non-CA group (figure 6E,F). We also observed a significant increase in the ratio of CD8⁺ T cells to Tregs in the CA+anti-PD-1 group compared with that in the non-CA group (figure 6G,H). Furthermore, the percentage of IFN- γ ⁺CD8⁺ and TNF- α ⁺CD8⁺ T cells in the CA+anti-PD-1 group was significantly higher than that in the other groups (figure 6I-L). These data suggest that blockade of the PD-L1/PD-1 pathway further boosts cryoablation-induced antitumor immune responses and reverses immune suppression at distant tumor sites.

Cryoablation combined with immune checkpoint blockade induces enhanced synergetic antitumor response in human NSCLC

Since the synergistic efficacy of the combination therapy was confirmed in animal experiments, we further validated the therapeutic efficacy in six immunotherapy-naïve patients with unresectable NSCLC. The baseline characteristics of the patients and their tumors are summarized in table 1. All tumors had a definite pathological diagnosis prior to the combined therapy, including two squamous cell carcinomas and four adenocarcinomas without any druggable mutations. These patients were ineligible for surgery due to deteriorated lung function, advanced disease, or refusal to undergo surgery. Cryoablation combined with anti-PD-1 treatment was then performed. During the follow-up period, we observed a reduction in tumor size of the targeted lesions on CT scans, as shown in figure 7A. Four patients achieved partial response, with an overall response rate of 66.7%, and are still being followed up. Two patients developed partial progression late in treatment due to irregular immunotherapy administration or incomplete cryoablation. Furthermore, we obtained tumor biopsies before and after the combined therapy from three patients and analyzed the TME using multiple-color fluorescence immunohistochemistry. We detected that CD8⁺ TIL infiltration increased in the target lesions after receiving the combined therapy (figure 7B).

In summary, our results further demonstrate that local cryoablation could help improve CD8⁺ TIL infiltration, thereby augmenting the effect of PD-L1/PD-1 blockade in the clinical treatment of NSCLC.

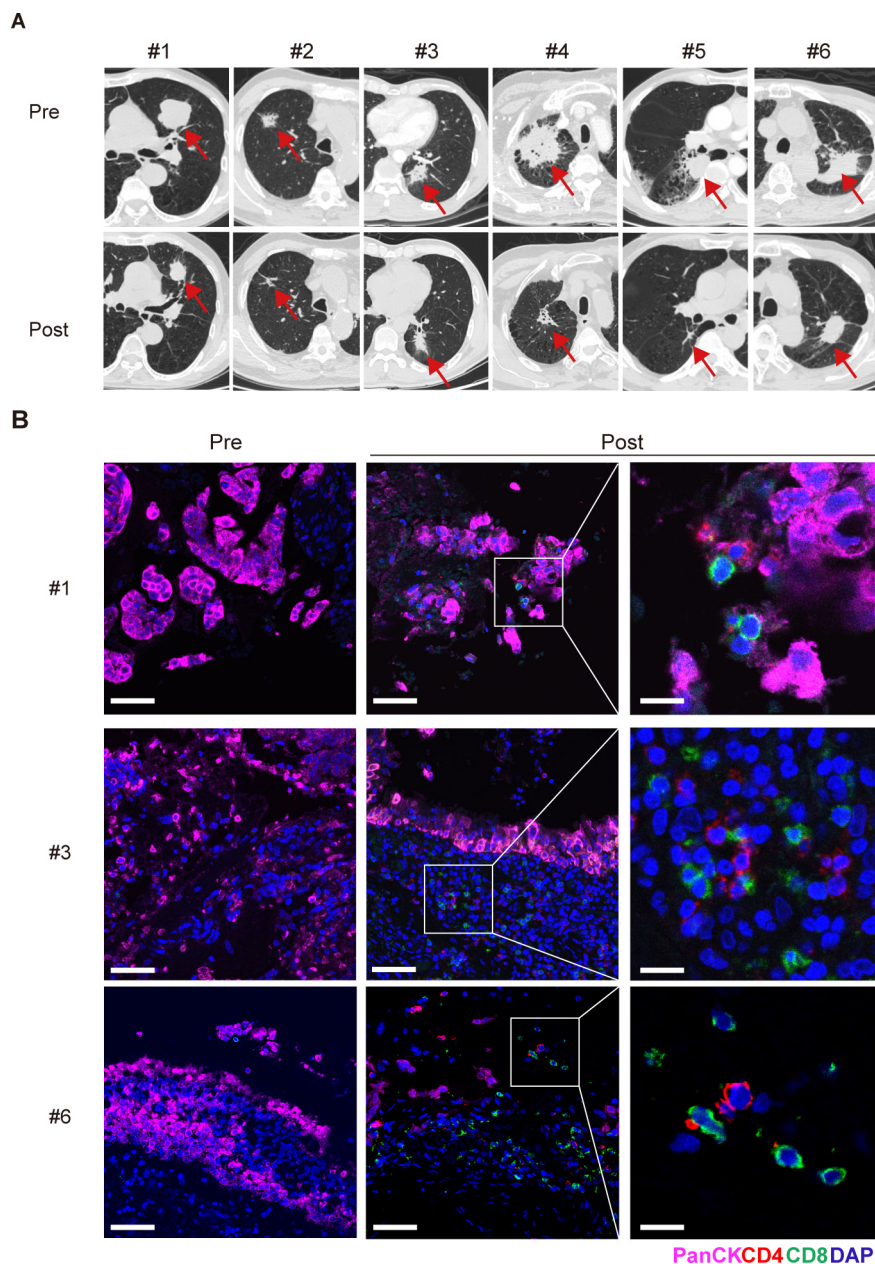


Figure 7 Cryoablation combined with immune checkpoint blockade induces synergistic antitumor responses in human NSCLC. (A) Representative CT scans of six patients who underwent cryoablation combined with anti-PD-1. The red arrows indicate the target lesions. Upper: CT before the combined therapy; lower: latest CT after the combined therapy (1: 12-month follow-up; 2: 44-month follow-up; 3: 5-month follow-up; 4 and 6: 9-month follow-up; 5: 14-month follow-up). (B) Representative immunofluorescence staining of tumor microenvironment in three paired biopsy specimens obtained before and after cryoimmunotherapy. Scale bar: 50 μm (left and middle) and 200 μm (right). NSCLC, non-small cell lung cancer; PD-1, programmed cell death protein 1.

DISCUSSION

Cryoablation has become even more popular because of its abscopal immune-regulatory effects, and recent investigations have aimed to explore the subsequent effect of immunological responses induced by cryoablation. In our study, we observed enrichment of CD8⁺ T lymphocytes and increased levels of inflammation-related cytokines in the peripheral blood of patients with NSCLC after cryoablation, indicating modified systemic immunity. We then employed the KP cell allograft mouse model to observe the cryoablation-induced abscopal immune response

and found that cryoablation induced tumor growth inhibition and extensive intratumoral immune cell infiltration in contralateral, non-ablated tumors. Therefore, it is hypothesized that cryoablation may induce a greater postablation immune response, altering the TME from an immune desert state into an inflammatory immune infiltration state, thus significantly enhancing antitumor immunity of the whole body.

It has been reported that cryoablation can preserve the immunogenicity of tumor antigens and facilitate the release of undamaged self-antigens into circulation.^{20 21}

However, the exact effects of cryoablation on the composition and function of intratumoral immune cells remain to be deciphered. In the current work, we provided a comprehensive single-cell transcriptome atlas to characterize the potential impacts of cryoablation on the immune states and cell transitions of CD45⁺ tumor-infiltrating immune cells. Our analysis revealed that cryoablation expanded CD8⁺ T cells with activation and effector features, including a population of initially activated T cells. Interestingly, we identified specific T cell subclusters with high expression of ISGs, which were mostly enriched in the CA group, and GO enrichment analysis demonstrated upregulation of the type I IFN-related pathway. These data suggest that activation of type I IFN signaling pathway may play a crucial role in cryoablation-induced antitumor immunity.

In recent research, type I IFNs, originally identified as potent defensive factors produced by our physiological and immune barriers to combat microbial infections, have been found to facilitate effective host immunological responses to tumor cells.^{22–23} Although it is known that various cell types can generate type I IFNs, the specific cells acting as primary type I IFN producers in the TME remain to be conclusively identified. Emerging evidence indicates that tumor-infiltrating CD11b⁺ DCs play a crucial role in producing type I IFNs in TME, triggered by the activation of tumor-derived DNA-sensing cGAS–STING pathway.^{24–25} In our study, we observed increased expression of IFN- α and IFN- β in the plasma of patients with NSCLC and contralateral murine tumors after cryoablation. To find out the primary type I IFN producer, we analyzed the activity of type I IFN production in different cell types using scRNA-seq data and found that monocytes and DCs may constitute the major source of type I IFNs in TME, which is consistent with prior studies.^{24–25} Previous studies revealed that tumor-derived DNA could trigger the activation of DNA-sensing cGAS–STING pathway, which is required for type I IFN production.^{26–27} Hence, we further detected the activation of STING pathway and found that cryoablation promoted STING phosphorylation. These data suggest that STING-dependent DNA sensing is critical for type I IFN production after cryoablation. Of note, except for innate immune cells, tumor cells can also produce type I IFNs.^{22–28–29} The reciprocal interaction related to type I IFN pathways between tumor and immune cells should be further investigated in future study as well. Additionally, type I IFN could further stimulate T cells by promoting maturation of T helper 1 cells, cytokine synthesis, and secretion of ISG chemokines to enhance antitumor effect.³⁰ Except for T cells, prior studies have shown that type I IFNs exert multiple impacts on various target cells within the TME,³¹ including NK cells,³² DCs,³³ neutrophils,^{34–35} Tregs,³⁶ and myeloid-derived suppressor cells.³⁷ In our study, we also found enhanced responses to type I IFNs in different subpopulations of T cells and myeloid cells from the CA group. Moreover, IFNAR1 blockade showed a negative effect on the inhibition of

tumor growth and CD8⁺ T cells infiltration in the TME induced by cryoablation. Collectively, these data suggest that STING-dependent type I IFN signaling activation plays an important role in the immune remodeling induced by cryoablation.

Recently, accumulating evidence indicates that type I IFNs have a synergistic effect with ICIs in the treatment of malignancies. Terawaki *et al.*³⁸ proposed that type I IFN-mediated PD-1 transcription might partially explain the attenuated T cell response in sustained immune reactions, which may also help explain the exhaustion features we observed in tumor-infiltrating CD8⁺ T cells at day 7 after cryoablation. Furthermore, the combination of type I IFN and PD-1 blockade effectively improved tumor control in mouse models.^{38–39} Recently, the combination of anti-PD-1 and type I IFN treatment has demonstrated promising clinical efficacy in metastatic melanoma and hepatocellular carcinoma with acceptable toxicity.^{40–41} Consequently, we hypothesized that cryoablation, which upregulates STING-dependent type I IFN responses, might act as the stimulus for type I IFNs, thereby amplifying the efficacy of combined therapies with PD-1 blockade immunotherapy.

However, the immunological effect induced by cryoablation alone may be insufficient for larger tumors. Various combination strategies that could amplify the abscopal effect of cryoablation have been investigated so far, such as combining cryoablation with adoptive cell transfer therapies^{42–43} or immunological adjuvants, such as CPG oligodeoxynucleotides.⁴⁴ Nowadays, the development of nanoplatform-based immunotherapy has become an innovative concept, potentially synergizing with cryoablation to amplify antitumor immunity.⁴⁵ Recently, immune checkpoint blockade has revolutionized the approach to cancer therapy, and ICIs treatment, either as monotherapy or combination therapy, has been established as the standard of care for patients with locally advanced or metastatic NSCLC without epidermal growth factor receptor (EGFR) or anaplastic lymphoma kinase (ALK) alterations.⁴⁶ Importantly, the addition of ICIs to cryoablation appeared to produce a more robust synergetic response compared with either ICIs or cryoablation alone, which has been observed in preclinical or clinical studies of several malignancies.^{10–11–47–50} Our study found that combining cryoablation with PD-1 blockade could induce a stronger immune response than either ablation or anti-PD-1 therapy alone. Our clinical data showed that the combined therapy benefited untreated patients with NSCLC and induce an elevated infiltration of CD8⁺ T cells in the TME, suggesting that the combination of cryoablation and ICIs is feasible and the synergetic therapeutic effect might be attributed to a CD8⁺ T cell response. Similar improved efficacy of the combined therapy of cryoablation and anti-PD-1 was also observed retrospectively in a relatively small cohort at the 12th week.⁵¹ In the future, further randomized controlled clinical trials with larger cohorts and longer follow-up are still warranted to systematically assess the clinical efficacy and

safety of cryoablation and anti-PD-1 combination therapy in patients with NSCLC.

Author affiliations

- ¹Department of Respiratory Endoscopy, Shanghai Chest Hospital, Shanghai Jiao Tong University School of Medicine, Shanghai, China
²Department of Respiratory and Critical Care Medicine, Shanghai Chest Hospital, Shanghai Jiao Tong University School of Medicine, Shanghai, China
³Shanghai Engineering Research Center of Respiratory Endoscopy, Shanghai, China
⁴State Key Laboratory of Cell Biology, Shanghai Institute of Biochemistry and Cell Biology, CAS Center for Excellence in Molecular Cell Science, Chinese Academy of Sciences, Shanghai, China
⁵University of Chinese Academy of Sciences, Beijing, China
⁶School of Life Science and Technology, ShanghaiTech University, Shanghai, China
⁷Key Laboratory of Systems Health Science of Zhejiang Province, School of Life Science, Hangzhou Institute for Advanced Study, University of Chinese Academy of Sciences, Chinese Academy of Sciences, Hangzhou, China
⁸Guangdong Institute of Intelligence Science and Technology, Hengqin, Zhuhai, Guangdong, China

Contributors CG: data curation, formal analysis, investigation, methodology, validation, visualization, writing—original draft, writing—review and editing. XW: data curation, formal analysis, methodology, validation, visualization, writing—review and editing. KW: data curation, formal analysis, methodology, validation, visualization, writing—original draft, writing—review and editing. FX: data curation, formal analysis, funding acquisition, investigation, writing—review and editing. LC: project administration, supervision, writing—review and editing. HJ: conceptualization, project administration, supervision, writing—review and editing. JS: conceptualization, funding acquisition, project administration, resources, supervision, writing—review and editing. JS is the guarantor of the content of the manuscript. The order of the co-first authors' names was determined on the basis of their relative contributions to the study.

Funding This study was supported by grants from the Nurture Projects for Basic Research of Shanghai Chest Hospital (2021YJJCQ4, 2019YJNCM10) and the National Multi-disciplinary Treatment Project for Major Diseases (2020NMDTP).

Competing interests None declared.

Patient consent for publication Not required.

Ethics approval This study involves human participants. The study protocols were approved by the Ethics Committee of Shanghai Chest Hospital (Shanghai, China) (KS2044, IS2010). These studies were conducted in accordance with the Declaration of Helsinki and the International Conference on Harmonization Guidelines for Good Clinical Practice. Participants gave informed consent to participate in the study before taking part. All animal experiments were performed in accordance with the protocols approved by the Institutional Committee for Animal Care and Use at Shanghai Chest Hospital (KS2045).

Provenance and peer review Not commissioned; externally peer reviewed.

Data availability statement Data are available from the corresponding author upon reasonable request.

Supplemental material This content has been supplied by the author(s). It has not been vetted by BMJ Publishing Group Limited (BMJ) and may not have been peer-reviewed. Any opinions or recommendations discussed are solely those of the author(s) and are not endorsed by BMJ. BMJ disclaims all liability and responsibility arising from any reliance placed on the content. Where the content includes any translated material, BMJ does not warrant the accuracy and reliability of the translations (including but not limited to local regulations, clinical guidelines, terminology, drug names and drug dosages), and is not responsible for any error and/or omissions arising from translation and adaptation or otherwise.

Open access This is an open access article distributed in accordance with the Creative Commons Attribution Non Commercial (CC BY-NC 4.0) license, which permits others to distribute, remix, adapt, build upon this work non-commercially, and license their derivative works on different terms, provided the original work is properly cited, appropriate credit is given, any changes made indicated, and the use is non-commercial. See <http://creativecommons.org/licenses/by-nc/4.0/>.

ORCID iD

Jiayuan Sun <http://orcid.org/0000-0003-3158-3256>

REFERENCES

- Sung H, Ferlay J, Siegel RL, *et al.* Global cancer Statistics 2020: GLOBOCAN estimates of incidence and mortality worldwide for 36 cancers in 185 countries. *CA Cancer J Clin* 2021;71:209–49.
- Venturini M, Cariati M, Marra P, *et al.* CIRSE standards of practice on thermal ablation of primary and secondary lung tumours. *Cardiovasc Intervent Radiol* 2020;43:667–83.
- Genshaft SJ, Suh RD, Abtin F, *et al.* Society of Interventional Radiology Multidisciplinary position statement on percutaneous ablation of non-small cell lung cancer and metastatic disease to the lungs: endorsed by the Canadian Association for Interventional Radiology, the cardiovascular and Interventional radiological society of Europe, and the society of Interventional oncology. *J Vasc Interv Radiol* 2021;32:S1051-0443(21)01082-4.
- Murphy MC, Wrobel MM, Fisher DA, *et al.* Update on image-guided thermal lung ablation: society guidelines, therapeutic alternatives, and Postablation imaging findings. *American Journal of Roentgenology* 2022;219:471–85.
- Chan MV, Huo YR, Cao C, *et al.* Survival outcomes for surgical resection versus CT-guided percutaneous ablation for stage I non-small cell lung cancer (NSCLC): a systematic review and meta-analysis. *Eur Radiol* 2021;31:5421–33.
- Liang L, Li G, Xie S, *et al.* Choice of treatment for stage IA non-small cell lung cancer patients ineligible for surgery: ablation or stereotactic body radiotherapy. *J Cancer* 2020;11:1634–40.
- Palussiè J, Catena V, Lagarde P, *et al.* Primary tumors of the lung: should we consider thermal ablation as a valid therapeutic option. *Int J Hyperthermia* 2019;36:46–52.
- Chu KF, Dupuy DE. Thermal ablation of tumours: biological mechanisms and advances in therapy. *Nat Rev Cancer* 2014;14:199–208.
- Gursel E, Roberts M, Veenema RJ. Regression of Prostatic cancer following sequential Cryotherapy to the prostate. *J Urol* 1972;108:928–32.
- Zhu C, Lin S, Liang J, *et al.* PD-1 blockade enhances the anti-tumor immune response induced by Cryoablation in a murine model of renal cell carcinoma. *Cryobiology* 2019;87:86–90.
- Benzon B, Glavaris SA, Simons BW, *et al.* Combining immune checkpoint blockade and Cryoablation in an immunocompetent hormone sensitive murine model of prostate cancer. *Prostate Cancer Prostatic Dis* 2018;21:126–36.
- Garon EB, Rizvi NA, Hui R, *et al.* Pembrolizumab for the treatment of non-small-cell lung cancer. *N Engl J Med* 2015;372:2018–28.
- Herbst RS, Baas P, Kim D-W, *et al.* Pembrolizumab versus Docetaxel for previously treated, PD-L1-positive, advanced non-small-cell lung cancer (KEYNOTE-010): a randomised controlled trial. *The Lancet* 2016;387:1540–50.
- Hu H, Khodadadi-Jamayran A, Dolgalev I, *et al.* Targeting the Atf7Ip-Setdb1 complex augments antitumor immunity by boosting tumor immunogenicity. *Cancer Immunol Res* 2021;9:1298–315.
- Wang X, Wang Y, Fang Z, *et al.* Targeting Hspa1A in Arid2-deficient lung adenocarcinoma. *Natl Sci Rev* 2021;8:wab014.
- Andreatta M, Corria-Osorio J, Müller S, *et al.* Interpretation of T cell States from single-cell Transcriptomics data using reference Atlases. *Nat Commun* 2021;12:2965.
- Gong L, Kwong DL-W, Dai W, *et al.* Comprehensive single-cell sequencing reveals the Stromal Dynamics and tumor-specific characteristics in the Microenvironment of Nasopharyngeal carcinoma. *Nat Commun* 2021;12:1540.
- Schattgen SA, Guion K, Crawford JC, *et al.* Integrating T cell receptor sequences and transcriptional profiles by Clonotype neighbor graph analysis (Conga). *Nat Biotechnol* 2022;40:54–63.
- Deng L, Liang H, Xu M, *et al.* STING-dependent cytosolic DNA sensing promotes radiation-induced type I interferon-dependent antitumor immunity in Immunogenic tumors. *Immunity* 2014;41:843–52.
- Luo X-M, Niu L-Z, Chen J-B, *et al.* Advances in Cryoablation for Pancreatic cancer. *World J Gastroenterol* 2016;22:790–800.
- Aarts BM, Klompenhouwer EG, Rice SL, *et al.* Cryoablation and Immunotherapy: an overview of evidence on its synergy. *Insights Imaging* 2019;10:53.
- Sistigu A, Yamazaki T, Vacchelli E, *et al.* Cancer cell-autonomous contribution of type I interferon signaling to the efficacy of chemotherapy. *Nat Med* 2014;20:1301–9.
- Zhang F, Manna S, Pop LM, *et al.* Type I interferon response in radiation-induced anti-tumor immunity. *Semin Radiat Oncol* 2020;30:129–38.
- Woo S-R, Fuertes MB, Corrales L, *et al.* STING-dependent cytosolic DNA sensing mediates innate immune recognition of Immunogenic tumors. *Immunity* 2014;41:830–42.

- 25 Andzinski L, Spanier J, Kasnitz N, *et al.* Growing tumors induce a local STING dependent type I IFN response in Dendritic cells. *Int J Cancer* 2016;139:1350–7.
- 26 Chen Q, Sun L, Chen ZJ. Regulation and function of the cGAS-STING pathway of cytosolic DNA sensing. *Nat Immunol* 2016;17:1142–9.
- 27 Hu Z, Teng X-L, Zhang T, *et al.* Senp3 senses oxidative stress to facilitate STING-dependent Dendritic cell antitumor function. *Mol Cell* 2021;81:940–52.
- 28 Núñez NG, Andreani V, Crespo MI, *et al.* IFN β produced by Tlr4-activated tumor cells is involved in improving the antitumoral immune response. *Cancer Res* 2012;72:592–603.
- 29 Parker BS, Rautela J, Hertzog PJ. Antitumour actions of Interferons: implications for cancer therapy. *Nat Rev Cancer* 2016;16:131–44.
- 30 Borden EC. Interferons α and β in cancer: therapeutic opportunities from new insights. *Nat Rev Drug Discov* 2019;18:219–34.
- 31 Yu R, Zhu B, Chen D. Type I interferon-mediated tumor immunity and its role in Immunotherapy. *Cell Mol Life Sci* 2022;79:191.
- 32 Marcus A, Mao AJ, Lensink-Vasan M, *et al.* Tumor-derived cGAMP triggers a STING-mediated interferon response in non-tumor cells to activate the NK cell response. *Immunity* 2018;49:754–63.
- 33 Duong E, Fessenden TB, Lutz E, *et al.* Type I interferon activates MHC class I-dressed Cd11b(+) conventional Dendritic cells to promote protective anti-tumor Cd8(+) T cell immunity. *Immunity* 2022;55:308–323.
- 34 Andzinski L, Kasnitz N, Stahnke S, *et al.* Type I Ifns induce anti-tumor polarization of tumor associated neutrophils in mice and human. *Int J Cancer* 2016;138:1982–93.
- 35 Jaillon S, Ponzetta A, Di Mitri D, *et al.* Neutrophil diversity and plasticity in tumour progression and therapy. *Nat Rev Cancer* 2020;20:485–503.
- 36 Hirata A, Hashimoto H, Shibasaki C, *et al.* Intratumoral IFN- α gene delivery reduces tumor-infiltrating regulatory T cells through the downregulation of tumor CCL17 expression. *Cancer Gene Ther* 2019;26:334–43.
- 37 Chen J, Sun H-W, Yang Y-Y, *et al.* Reprogramming immunosuppressive myeloid cells by activated T cells promotes the response to anti-PD-1 therapy in colorectal cancer. *Signal Transduct Target Ther* 2021;6:4.
- 38 Terawaki S, Chikuma S, Shibayama S, *et al.* IFN- α directly promotes programmed cell death-1 transcription and limits the duration of T cell-mediated immunity. *J Immunol* 2011;186:2772–9.
- 39 Liang Y, Tang H, Guo J, *et al.* Targeting IFN α to tumor by anti-PD-L1 creates feedforward antitumor responses to overcome checkpoint blockade resistance. *Nat Commun* 2018;9:4586.
- 40 Davar D, Wang H, Chauvin J-M, *et al.* Phase IB/II study of Pembrolizumab and pegylated-interferon Alfa-2B in advanced Melanoma. *J Clin Oncol* 2018;36:JCO1800632.
- 41 Hu B, Yu M, Ma X, *et al.* IFN α Potentiates Anti-PD-1 Efficacy by Remodeling Glucose Metabolism in the Hepatocellular Carcinoma Microenvironment. *Cancer Discov* 2022;12:1718–41.
- 42 Yuanying Y, Lizhi N, Feng M, *et al.* Therapeutic outcomes of combining Cryotherapy, chemotherapy and DC-CIK Immunotherapy in the treatment of metastatic non-small cell lung cancer. *Cryobiology* 2013;67:235–40.
- 43 Lin M, Liang S-Z, Wang X-H, *et al.* Clinical efficacy of percutaneous Cryoablation combined with Allogenic NK cell Immunotherapy for advanced non-small cell lung cancer. *Immunol Res* 2017;65:880–7.
- 44 Zhang M, Yin T, Lu Y, *et al.* The application of Cytidyl Guanosyl Oligodeoxynucleotide can affect the antitumor immune response induced by a combined protocol of Cryoablation and Dendritic cells in Lewis lung cancer model. *Med Sci Monit* 2016;22:1309–17.
- 45 Yu Z, Wang D, Qi Y, *et al.* Autologous-cancer-Cryoablation-mediated Nanovaccine augments systematic Immunotherapy. *Mater Horiz* 2023;10:1661–77.
- 46 Reck M, Remon J, Hellmann MD. First-line Immunotherapy for non-small-cell lung cancer. *JCO* 2022;40:586–97.
- 47 Waitz R, Solomon SB, Petre EN, *et al.* Potent induction of tumor immunity by combining tumor Cryoablation with anti-CTLA-4 therapy. *Cancer Res* 2012;72:430–9.
- 48 Soule E, Bandyk M, Matteo J. Percutaneous Ablative Cryoimmunotherapy for Micrometastatic Abscopal effect: no complications. *Cryobiology* 2018;82:22–6.
- 49 McArthur HL, Diab A, Page DB, *et al.* A pilot study of preoperative single-dose Ipilimumab and/or Cryoablation in women with early-stage breast cancer with comprehensive immune profiling. *Clin Cancer Res* 2016;22:5729–37.
- 50 Tan J, Liu T, Fan W, *et al.* Anti-PD-L1 antibody enhances curative effect of Cryoablation via antibody-dependent cell-mediated cytotoxicity mediating PD-L1(High)Cd11b(+) cells elimination in hepatocellular carcinoma. *Acta Pharmaceutica Sinica B* 2023;13:632–47.
- 51 Feng J, Guiyu D, Xiongwen W. The clinical efficacy of argon-helium knife Cryoablation combined with Nivolumab in the treatment of advanced non-small cell lung cancer. *Cryobiology* 2021;102:92–6.

1 **Supplementary Methods**

2 **Mouse lung cancer allograft assay and treatments**

3 A total of 1×10^6 KP, KL or LLC cells were injected subcutaneously into the bilateral flanks of
4 female C57BL/6 mice, respectively. The treatment was administered when the tumor volume
5 (calculated as width \times length) reached approximately 50 mm². All cryoablation procedures were
6 carried out only on the left tumor, using the Cryotherapy System device and a 1.2-mm-diameter
7 cryoprobe (AccuTarget MediPharma [Shanghai] Co., Ltd.), which used nitrogen as the refrigerant.
8 The tip of the cryoprobe was inserted into the tumor along its long axis, and then 2 freeze-thaw
9 cycles (20 and 10 seconds, respectively, for each cycle) were performed. During the freezing
10 phase, the temperature at the tip of the cryoprobe could reached below -80°C. The target tumor
11 was entirely covered by the ice ball to ensure complete ablation. The growth of contralateral
12 tumors was monitored every 2 days.

13 IFNAR1 blockade was accomplished by administering 400 μ g anti-IFNAR1 (clone MAR1-5A3,
14 BioXCell) or isotype control monoclonal antibody (BioXCell) intraperitoneally every 3 days for a
15 total of 4 doses. For PD-1 blockade, 200 μ g anti-PD-1 (clone MP1-14, BioXCell) or isotype
16 control monoclonal antibody (BioXCell) was administered intraperitoneally at day 1, 4, 7 and 10
17 after cryoablation (figure 6B).

18

19 **Sham treatment and cryoablation**

20 The treatment was administered when the tumor volume (calculated as width \times length) reached
21 approximately 50 mm². The experimental grouping is shown in supplementary figure S2A. In
22 non-CA group, no treatment was received. In sham treatment group, cryoprobe was inserted into

23 the left tumor without cryoablation. In sham CA group, CA was performed in subcutaneous tissue
24 ensuring no damage to the implanted tumor. In CA group, CA was performed in tumor tissues.
25 The growth of contralateral tumors was monitored every 2 days.

26

27 **Data analysis for bulk RNA sequencing**

28 Genome index and raw gene expression matrix for each sample were generated from raw fastq
29 data using *STAR* (v2.7.6a) [1]. The combined gene expression matrix was then generated by
30 customized scripts for *R* (v4.1.3). Subsequently, the gene expression matrix was converted to a
31 *DESeqDataSet* object using *DESeq2* R package (v1.34.0) [2]. Normalization was performed by
32 *DESeq2* and DEGs were selected by adjusted p-value < 0.05. Gene set signatures were computed
33 using the average gene expression and *GSVA* (v1.42.0) R package based on Hallmark gene sets
34 (h.all.v7.4.symbols.gmt) and some manually curated pathways. To visualize gene expression and
35 gene set activity, the heatmaps were generated using *ComplexHeatmap* R package (v2.10.0) [3].

36

37 **Flow cytometric analysis**

38 *Preparation of mouse tumors*

39 Freshly harvested tumors were treated with the Mouse Tumor Dissociation Kit (Miltenyi Biotec)
40 to generate single-cell suspension for flow cytometry following the manufacturer's instructions.
41 Subsequently, the dissociated tumor samples were filtered through a 70- μ m strainer, followed by
42 centrifugation using Percoll reagent (GE) to enrich immune cells. Erythrocytes were lysed with
43 lysis buffer (Beyotime) for 5 min at RT and washed twice with PBS.

44 *Staining*

45 To detect intracellular cytokine production, cells were stimulated with Cell Stimulation Cocktail
46 (plus protein transport inhibitors) (1:500, eBioscience) for 4 hours in a 37°C and 5% CO₂
47 incubator, and washed twice with FACS buffer (PBS + 2% FBS + 1mM EDTA) before staining.
48 For live-dead discrimination, cells were stained with Zombie UV™ Fixable Viability Kit
49 (Biolegend) for 30 min at RT in the dark. For surface marker analysis, cells were stained with
50 indicated fluorochrome-conjugated antibodies in FACS buffer for 30 minutes. For intracellular
51 marker staining, the Transcription Factor Buffer Set (BD Pharmingen) was utilized following the
52 manufacturer's instructions, and then stained with indicated fluorochrome-conjugated antibodies.
53 All samples were washed with washing buffer (BD Pharmingen) after each staining. At last, all
54 samples further passed through a 70-µm cell strainer. The antibodies used for flow cytometry
55 staining were listed in supplemental table S2. Flow cytometry was performed using BD FACS
56 Fortessa. Data were analyzed with FlowJo 10.8.1 software. Appropriate isotype controls were used
57 as negative controls.

58

59 **Quality control, determination of major cell lineages and subclustering of T cells and**
60 **myeloid populations**

61 *Cell Ranger* (v6.0.1) *count* was used to aggregate the raw gene expression matrix from the initial
62 raw fastq data of each sample, which was converted to a Seurat object using *Seurat* R package
63 (v4.1.1) [4]. The gene expression was normalized by the SCT method [5] and a total of 17,670 and
64 40,917 high-quality cells were finally obtained for CD45⁺ and CD45⁺CD3⁺ scRNA-seq
65 respectively. Cell clusters projected in the two-dimensional *UMAP* representation were annotated
66 to known cell types using well-recognized marker genes.

67 To further identify subpopulations within the major cell clusters from CD45⁺ 3' scRNA-seq, a
68 second-round data process, dimension reduction and cell type annotation were performed for T
69 and myeloid cells separately. The subset gene expression matrix was normalized by the
70 *LogNormalize* method, and a total of 12 subclusters were obtained. To validate the accuracy of our
71 annotation results, *ProjectTIL* analysis [6] (*ProjectTILs* R package, v2.0.0) was performed with the
72 'mouse TIL atlas' as a reference atlas, and most of cell types were well-matched. Myeloid cells,
73 including mast cells, underwent a similar re-clustering pipeline as T cells, resulting in the
74 identification of 8 clusters.

75

76 **Analysis of pathway enrichment and gene signatures**

77 DEGs were identified using the Wilcoxon Rank Sum test between the non-CA and CA groups,
78 either across all cells or within specific cell clusters by *Seurat* R package with default parameters.
79 A maximum of 120 DEGs with a logFC_threshold > 0.25 were selected. GO enrichment analysis
80 was performed with *clusterProfiler* R package (v4.2.2) based on the up-regulated DEGs in the CA
81 group. The results were visualized through barplots generated by *ggplot2* R package (v3.4.1).

82 Gene set signatures from both bulk RNA-seq and 3' scRNA-seq, including the effector
83 signature, cytolytic score and IFN response signature of CD8⁺ T cells, and type I IFN production
84 were computed using the average gene expression and *GSEA* (v1.42.0) R package based on
85 Hallmark gene sets (h.all.v7.4.symbols.gmt), GO gene sets (c5.go.v7.4.symbols.gmt) from
86 MSigDB and some manually curated pathways. Naïve and exhaustion scores of CD8⁺ T cells were
87 performed by a customized R script, following the methodology established by Gong et al [7]. In
88 brief, logistic regression models were developed for each gene module and corresponding cell

89 clusters, and then the module score for each cell was calculated by summing the product of each
90 gene expression and weights estimated from the model parameters. The heatmap was plotted using
91 *ComplexHeatmap* with P-value and Z-score computed by R, and the boxplots were plotted using
92 *ggplot2* with statistical tests performed by *ggpubr* R package (v0.4.0).

93

94 **Pseudotime trajectory analysis of CD8⁺ T cells and myeloid populations**

95 Pseudotime trajectory analysis of CD8⁺ T cells was performed by *Monocle v3* R package (v1.0.0)
96 [8]. Pseudotime values were calculated, and the trajectory paths and directions were computed.
97 *Monocle v3* and *ggplot2* R package were used to visualize the pseudotime trajectory. Pseudotime
98 trajectory analysis of Myeloid cells was performed by *Monocle v2* R package (v2.22.0) [9]. The
99 two-dimensional components and pseudotime values by *Monocle v2* were merged into the Seurat
100 object, and *Seurat* and *ggplot2* were used to visualize the pseudotime trajectory.

101

102 **Clonotype diversity analysis and CoNGA**

103 *Immunarch* R package (v0.8.0) was applied to read and process the clonotype data from outputs of
104 *CellRanger vdj*. The clonotype data was then integrated with cell attributes from scRNA-seq data
105 based on shared cell barcodes. The clonal expansion score, as defined by Wang et al. [10], was
106 calculated and compared in T cell clusters between non-CA and CA groups.

107 To enhance the integration of information between scRNA-seq and scTCR-seq, we performed
108 *CoNGA* (*CoNGA* python package, v0.1) analysis [11]. In brief, CoNGA uses TCRdist to cluster
109 immune repertoire (IR) data and generate a cell-cell relationship network from the IR.
110 Simultaneously, it generates a cell-cell relationship network from gene expression (GEX) using

111 Scanpy. Subsequently, CoNGA integrates the GEX and IR networks by identifying nodes that
112 share similar neighbors in both networks. By employing CoNGA approach, we acquired 23,739
113 paired cells which was reduced into 15,055 clones. Each clone was assigned a CoNGA score
114 through the *CoNGA* pipeline.

115

116 **Multiplex immunoassay**

117 The mouse tumor tissues were homogenized (1:9) in PBS for 4 minutes, and then were centrifuged
118 at 12,000 rpm for 5 minutes at 4°C. Supernatants were collected and the protein level of IFN- α
119 and IFN- β was detected using LEGENDplex™ Mouse Type 1/2 Interferon Panel (Biolegend)
120 according to the manufacturer's instructions. Briefly, 25 μ l supernatant or standard was mixed with
121 25 μ l assay buffer and mixed capture beads, and then incubated for 2 hours at room temperature.
122 After washing the plate, 25 μ l detection antibodies were added to each well and incubated for 1
123 hour at room temperature. Then SA-PE was added directly and incubated for 30 min at room
124 temperature. After washing, all samples were read on Beckman Coulter CytoFLEX S. The assay
125 FCS files were analyzed to calculate the concentration of IFN- α and IFN- β using BioLegend's
126 LEGENDplex™ data analysis software.

127

128 **Western blot analysis**

129 Mouse tumor tissues were lysed using RIPA lysis buffer (P0013B, Beyotime) containing a
130 protease inhibitor (1:100, Beyotime) and a phosphatase inhibitor (1:100, Epizyme).
131 Approximately 30–50 μ g of total protein was separated on 10% SDS-PAGE, transferred onto a
132 0.45- μ m PVDF membrane, blocked with 5% non-fat milk, and incubated overnight at 4 °C with

133 primary antibodies against indicated antibodies (supplementary table S2). Antibodies were
134 removed from the membrane by incubation with stripping buffer (Beyotime) for 15 min.

135

136 **Statistics**

137 All statistical analyses in the experiments were performed using SPSS 25.0 (IBM, New York, NY,
138 USA) and GraphPad Prism 8.0 (GraphPad Software, San Diego, California, USA). P -value ≤ 0.05
139 was considered significant difference. Data are expressed as mean \pm SEM. The two-sided unpaired
140 Student's t -test was used for comparison of two groups (non-CA and CA group; before and after
141 the cryoablation). ANOVA test was used for comparisons of groups in studies involving combined
142 therapy (PD-1 blockade and IFNAR-1 blockade). Survival curves were analyzed by log-rank
143 (Mantel Cox) test.

144 All statistical analyses of omics data were performed using R (v4.1.3). Z-score normalization
145 was applied for better visualization in the heatmap. P -value ≤ 0.05 was considered significant
146 difference. The one-sided unpaired Student's t -test was used for comparison of gene expression
147 and signature scores between the non-CA and CA groups in bulk RNA-seq data. For single-cell
148 analysis, comparisons between two groups were performed using the nonparametric Wilcoxon
149 rank sum test with Bonferroni correction.

150

151 **References**

- 152 1. Dobin A, Davis CA, Schlesinger F et al. STAR: ultrafast universal RNA-seq aligner.
153 *Bioinformatics* 2013; 29: 15-21.
- 154 2. Anders S, Huber W. Differential expression analysis for sequence count data. *Genome Biol*

- 155 2010; 11: R106.
- 156 3. Gu Z, Eils R, Schlesner M. Complex heatmaps reveal patterns and correlations in
157 multidimensional genomic data. *Bioinformatics* (Oxford, England) 2016; 32: 2847-2849.
- 158 4. Hao Y, Hao S, Andersen-Nissen E, Mauck WM, 3rd, Zheng S, Butler A, et al. Integrated
159 analysis of multimodal single-cell data. *Cell*. 2021;184(13):3573-87 e29.
- 160 5. Hafemeister C, and Satija R. Normalization and variance stabilization of single-cell RNA-seq
161 data using regularized negative binomial regression. *Genome Biol*. 2019;20(1):296.
- 162 6. Andreatta M, Corria-Osorio J, Muller S, Cubas R, Coukos G, and Carmona SJ. Interpretation
163 of T cell states from single-cell transcriptomics data using reference atlases. *Nat Commun*.
164 2021;12(1):2965.
- 165 7. Gong L, Kwong DL, Dai W, Wu P, Li S, Yan Q, et al. Comprehensive single-cell sequencing
166 reveals the stromal dynamics and tumor-specific characteristics in the microenvironment of
167 nasopharyngeal carcinoma. *Nat Commun*. 2021;12(1):1540.
- 168 8. Cao J, Spielmann M, Qiu X, Huang X, Ibrahim DM, Hill AJ, et al. The single-cell
169 transcriptional landscape of mammalian organogenesis. *Nature*. 2019;566(7745):496-502.
- 170 9. Qiu X, Mao Q, Tang Y, Wang L, Chawla R, Pliner HA, et al. Reversed graph embedding
171 resolves complex single-cell trajectories. *Nat Methods*. 2017;14(10):979-82.
- 172 10. Wang J, Xu Y, Chen Z, Liang J, Lin Z, Liang H, et al. Liver Immune Profiling Reveals
173 Pathogenesis and Therapeutics for Biliary Atresia. *Cell*. 2020;183(7):1867-83 e26.
- 174 11. Schattgen SA, Guion K, Crawford JC, Souquette A, Barrio AM, Stubbington MJT, et al.
175 Integrating T cell receptor sequences and transcriptional profiles by clonotype neighbor graph
176 analysis (CoNGA). *Nat Biotechnol*. 2022;40(1):54-63.

177

Supplemental Table S1. Mouse primers used in this study

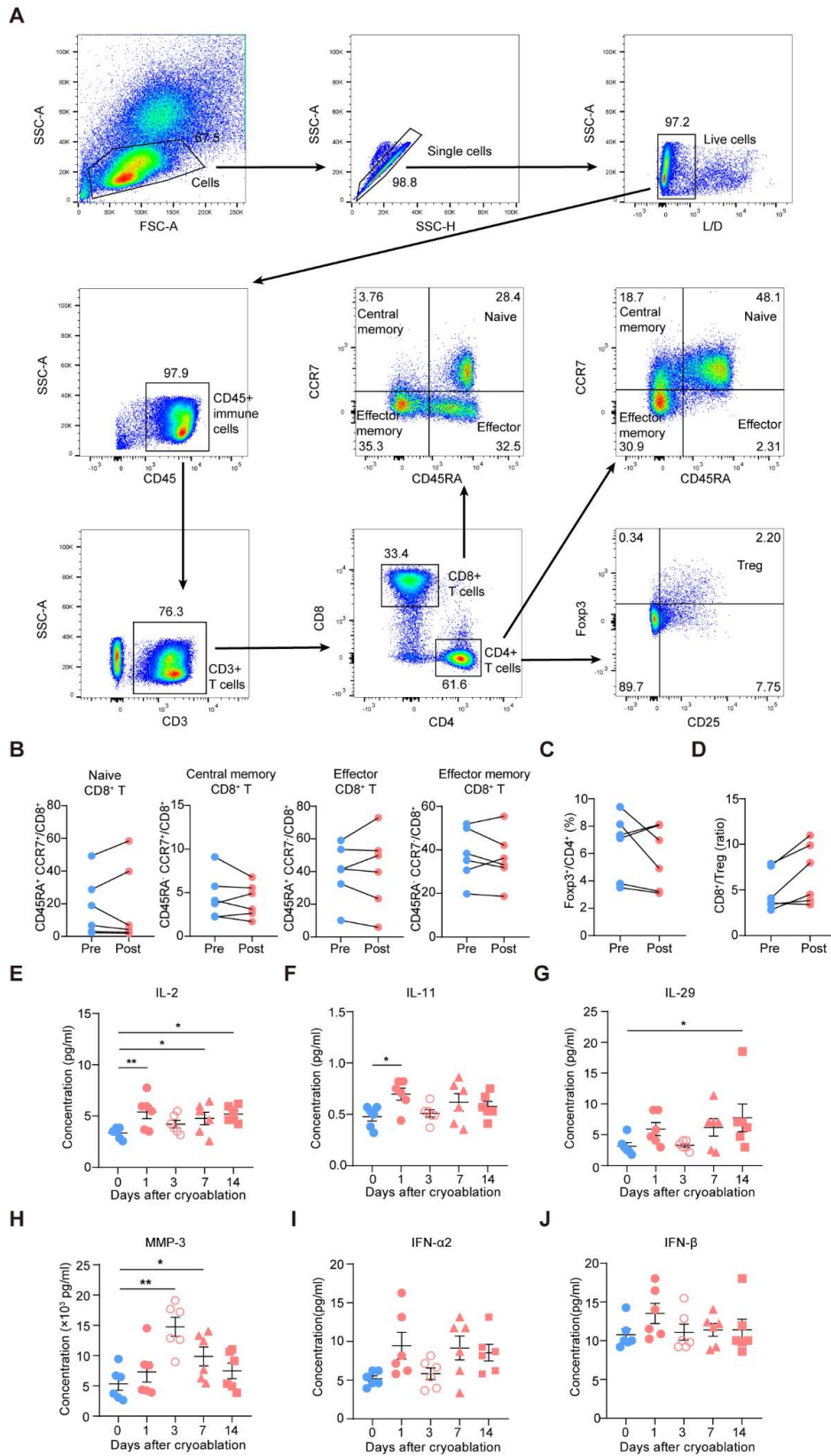
Gene	Forward Primer (5'-3')	Reverse Primer (5'-3')
<i>Il21</i>	GGACCCTTGTCTGTCTGGTAG	TGTGGAGCTGATAGAAGTTCAGG
<i>Ccl5</i>	GCTGCTTTGCCTACCTCTCC	TCGAGTGACAAACACGACTGC
<i>Ccl17</i>	TACCATGAGGTCACCTCAGATGC	GCACTCTCGGCCTACATTGG
<i>Ccl22</i>	AGGTCCCTATGGTGCCAATGT	CGGCAGGATTTTGAGGTCCA
<i>Cxc19</i>	GGAGTTCGAGGAACCCTAGTG	GGGATTTGTAGTGGATCGTGC
<i>Tnf</i>	CCCTCACACTCAGATCATCTTCT	GCTACGACGTGGGCTACAG
<i>Ifna</i>	TGACCTCAAAGCCTGTGTGATG	AAGTATTTCTCACAGCCAGCAG
<i>Ifnb</i>	AGCTCCAAGAAAGGACGAACAT	GCCCTGTAGGTGAGGTTGATCT
<i>Cd274</i>	GCTCCAAGGACTTGTACGTG	TGATCTGAAGGGCAGCATTTTC
<i>β-actin</i>	TGTCCACCTTCCAGCAGATGT	AGCTCAGTAACAGTCCGCCTAG

178

Supplemental Table S2. The antibodies used for flow cytometry, WB and multiple-color fluorescence IHC

Antibodies	Clone	Source	Identifier
Zombie UV™ Fixable Viability Kit	/	Biolegend	Cat# 423107
BV510 anti-mouse CD45	30-F11	Biolegend	Cat# 103138
AF700 anti-mouse CD3	17A2	Biolegend	Cat# 100216
FITC anti-mouse CD4	RM4-5	Biolegend	Cat# 100510
PerCP/Cyanine5.5 anti-mouse CD8a	53-6.7	Biolegend	Cat# 100734
BV605 anti-mouse NK1.1	PK136	Biolegend	Cat# 108753
BV605 anti-mouse PD-1	29F.1A12	Biolegend	Cat# 135220
BV421 anti-mouse CD25	PC61	Biolegend	Cat# 102043
PE anti-mouse FOXP3	NRRF-30	eBioscience	Cat# 12-4771-82
PE/Dazzle 594 anti-mouse IFN- γ	XMG1.2	Biolegend	Cat# 505846
PE anti-mouse TNF- α	MP6-XT22	Biolegend	Cat# 506306
PE/Cyanine7 anti-human/mouse Granzyme B	QA16A02	Biolegend	Cat# 372214
BV510 anti-human CD45	HI30	Biolegend	Cat# 304036
PerCP/Cyanine5.5 anti-human CD3	OKT3	Biolegend	Cat# 317226
AF700 anti-human CD4	OKT4	Biolegend	Cat# 317426
APC/Cyanine7 anti-human CD8	SK1	Biolegend	Cat# 344714
BV605 anti-human CD45RA	HI100	Biolegend	Cat# 304134
BV421 anti-human CD197 (CCR7)	G043H7	Biolegend	Cat# 353208
PE/Dazzl 594 anti-human FOXP3	206D	Biolegend	Cat# 320126
Rabbit anti-mouse p-STING (Ser365) mAb	D8W4F	CST	Cat# 72971
Rabbit anti-mouse STING mAb	D2P2F	CST	Cat# 13647
Rabbit anti-mouse p-TBK1/NAK (Ser172) mAb	D52C2	CST	Cat# 5483
Rabbit anti-mouse TBK1/NAK mAb	D1B4	CST	Cat# 3504
Rabbit anti-mouse β -Actin mAb	13E5	CST	Cat# 4970
Anti-rabbit IgG, HRP-linked Antibody	7074S	CST	Cat# 7074
Mouse monoclonal anti-human Pan-CK	AE1/AE3	Abcam	Cat# ab27988
Rabbit monoclonal anti-human CD4	EPR6855	Abcam	Cat# ab133616
Mouse monoclonal anti-human CD8 alpha	C8/144B	Abcam	Cat# ab17147

179



181 **Supplementary Figure S1. The effect of cryoablation on peripheral blood from early-stage**

182 **NSCLC patients.**

183 (A) The gating strategy of flow cytometric analysis on peripheral blood mononuclear cells.

184 (B-D) The changes in the percentage of subpopulations of CD8+ T cells (B), the percentage of

185 Foxp3+ Tregs (C) and the ratio of CD8+ T cells to Tregs (D) in the peripheral blood samples

186 collected before cryoablation and at day 1 after cryoablation from early-stage NSCLC patients (n

187 = 6).

188 (E-J) The changes in the levels of IL-2, IL-11, IL-29, MMP-3, IFN- α and IFN- β secretion in the

189 peripheral blood samples collected before cryoablation and at day 1, 3, 7 and 14 after cryoablation

190 from early-stage NSCLC patients (n = 6).

191 The results are shown as the mean \pm SEM. The statistical significance of differences between two

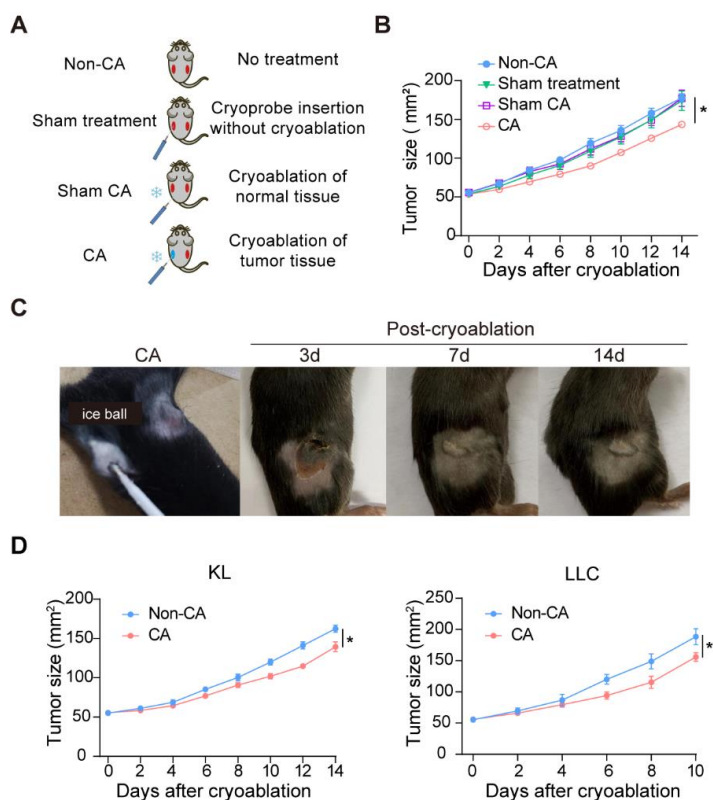
192 groups was determined by unpaired Student's t-test and the statistical significance of differences

193 among multiple groups was determined by one-way ANOVA. *, P < 0.05; **, P < 0.01. IL,

194 interleukin; IFN, interferon; MMP, matrix metalloproteinase; NSCLC, non-small cell lung cancer;

195 SSC, side scatter.

196



197

198 **Supplementary Figure S2. The effect of cryoablation on tumor growth.**

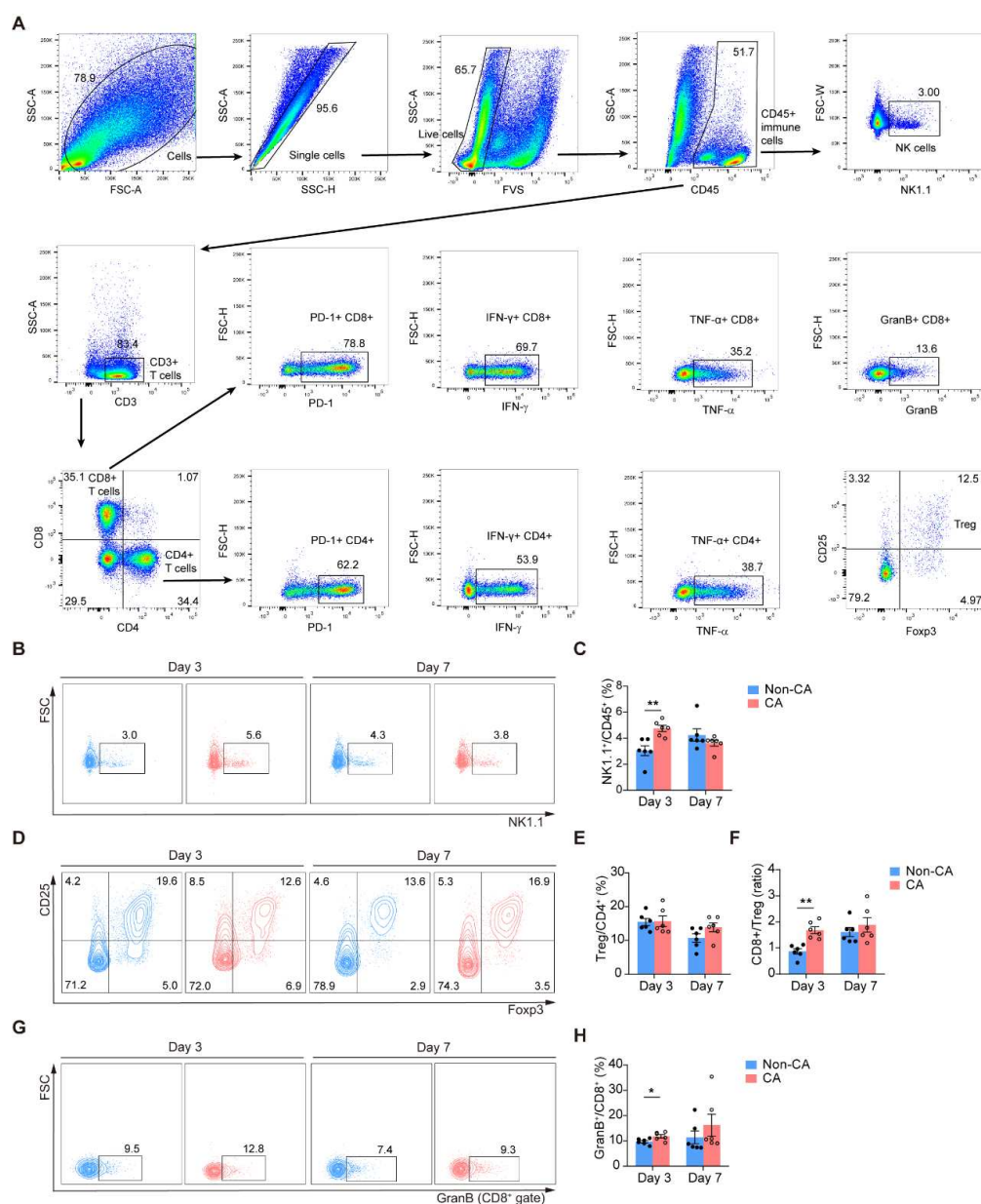
199 (A) The experimental design. In non-CA group, no treatment was received. In sham treatment
 200 group, the cryoprobe was inserted into the left tumor without cryoablation. In sham CA
 201 was performed in subcutaneous tissue and skin ensuring no damage to the implanted tumor. In CA
 202 group, CA was performed in tumor tissues.

203 (B) Mean tumor growth of the contralateral KP tumors in the non-CA, sham treatment, sham CA
 204 and CA groups (n=5 per group).

205 (C) The changes of the cryoablated tumor during cryoablation and at day 3, 7 and 14 after
 206 cryoablation.

207 (D) Mean tumor growth of the contralateral KL and Lewis lung cancer (LLC) tumors in the
 208 non-CA and CA groups (n = 6 per group).

209 The results are shown as the mean \pm SEM. The statistical significance of differences between two
210 groups was determined by unpaired Student's t-test. *, P < 0.05. CA, cryoablation; non-CA,
211 non-cryoablation.
212



213

214 **Supplementary Figure S3. Regulation of immune cell infiltration in contralateral KP tumors**215 **by cryoablation.**

216 (A) The gating strategy of flow cytometric analysis on KP tumor infiltrating immune cells.

217 (B and C) Representative flow cytometric plots (B) and the percentage (C) of NK1.1+ natural

218 killer (NK) cells in contralateral KP tumors from the non-CA and CA groups at day 3 and 7 after

219 cryoablation (n = 6 per group).

220 (D and E) Representative flow cytometric plots (D) and the percentage (E) of CD25+Foxp3+

221 Tregs in contralateral KP tumors from the non-CA and CA groups at day 3 and 7 after

222 cryoablation (n = 6 per group).

223 (F) The ratio of CD8+ TILs to Tregs in the non-CA and CA groups (n = 6 per group).

224 (G and H) Representative flow cytometric plots (G) and the percentage (H) of GranB+CD8+ TILs

225 in contralateral KP tumors from the non-CA and CA groups at day 3 and 7 after cryoablation (n =

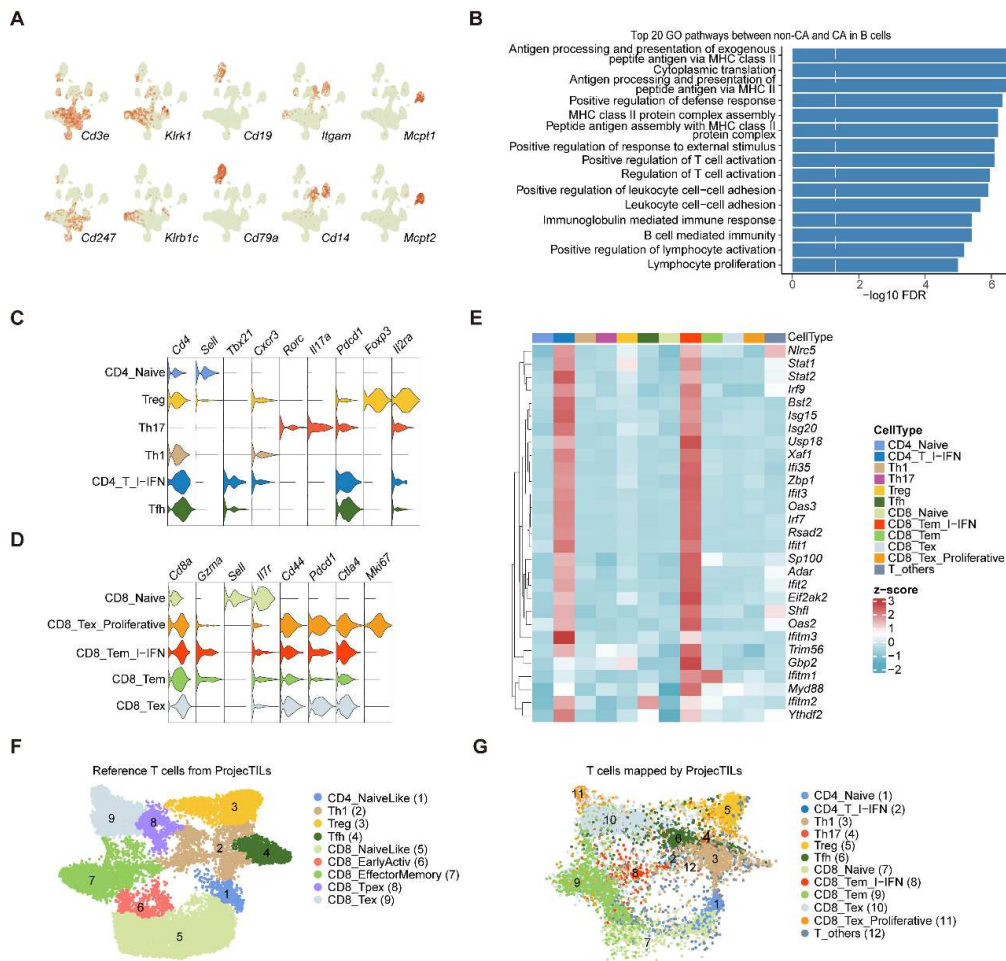
226 6 per group).

227 The results are shown as the mean \pm SEM, and the statistical significance of differences between

228 groups was determined by an unpaired Student's t-test. *, P < 0.05; **, P < 0.01. CA, cryoablation;

229 non-CA, non-cryoablation.

230



231

232 **Supplementary Figure S4. Transcriptional profiling of tumor-infiltrating immune cells.**

233 (A) Single-cell transcription level of representative genes illustrated in the UMAP plot of
 234 tumor-infiltrating CD45+ immune cells.

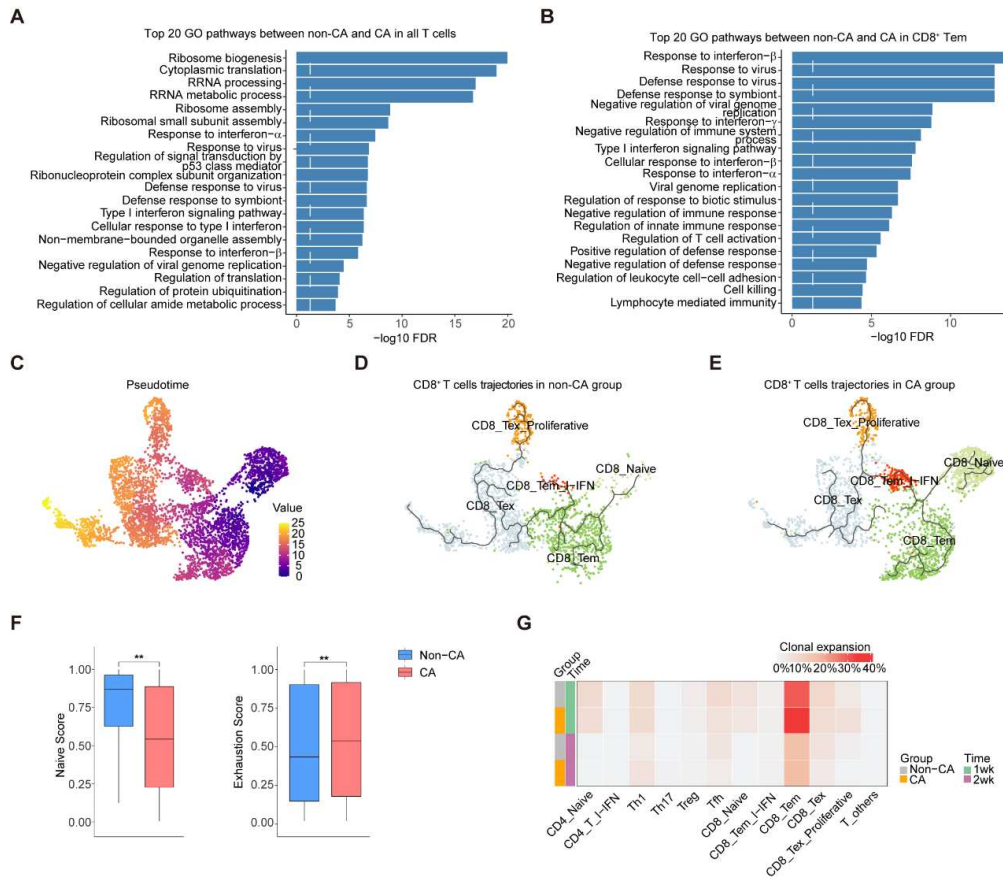
235 (B) GO pathway enrichment analysis of B cells based on the DEGs between the non-CA
 236 groups.

237 (C and D) Single-cell transcription level of representative genes from CD4+ (C) and CD8+ (D)
 238 TILs illustrated in the UMAP plot of CD3+CD45+ T cells.

239 (E) Heatmap showing expression of type I IFN-related genes in each T cell type.

240 (F and G) Validation of T cells clustering using ProjecTIL. The graphs represent a reference atlas

- 241 from ProjectTILs (F) and our clustering of T cells mapped by ProjectTILs (G).
- 242 CA, cryoablation; non-CA, non-cryoablation.
- 243



244

245 **Supplementary Figure S5. Expansion of T cells exhibiting upregulated responses to type I**246 **IFN pathway and exhaustion features post-cryoablation.**247 (A and B) GO pathway enrichment analysis of all T cells and CD8⁺ effector memory T cells based

248 on the DEGs between the non-CA and CA groups.

249 (C-E) The pseudotime developmental trajectory performed on CD8⁺ T cells. The graphs represent

250 pseudotime values (C), pseudotime trajectory in the non-CA (D) and CA (E) groups.

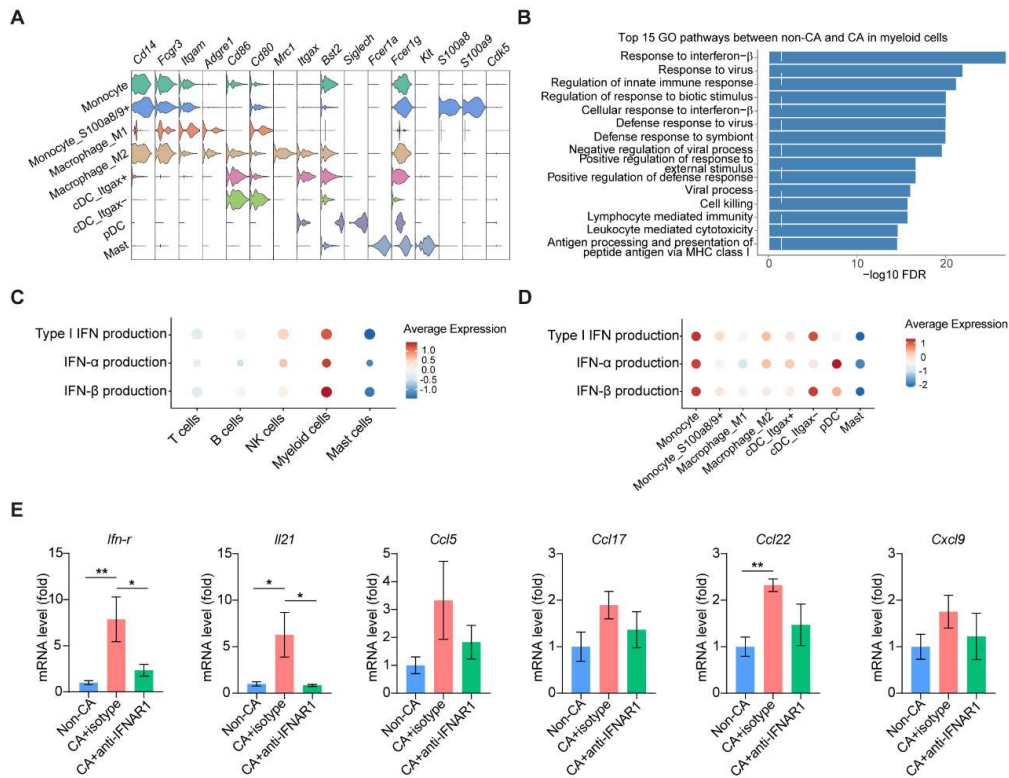
251 (F) Box plot indicating naïve and exhaustion scores of CD8⁺ T cells at 1 week after cryoablation.

252 (G) Heatmap showing clonal expansion in T cell clusters across groups at 1 week and 2 weeks

253 after cryoablation.

254 The statistical significance of differences between groups was determined by the nonparametric

255 Wilcoxon rank sum test with Bonferroni correction. **, $P < 0.01$. CA, cryoablation; non-CA,
256 non-cryoablation.
257



263

264 **Supplementary Figure S7. Upregulation of responses to type I IFN in myeloid cells after**265 **cryoablation and changes of intra-tumoral cytokines and chemokines upon IFNAR1**266 **blockade.**

267 (A) Single-cell transcription level of representative genes illustrated in the UMAP plot of myeloid

268 cells.

269 (B) GO pathway enrichment analysis of myeloid cells based on the DEGs between the non-CA

270 and CA groups.

271 (C and D) Type I IFN production analysis in different cell types (C) and subpopulations of

272 myeloid cells (D).

273 (E) mRNA levels of intra-tumoral cytokines and chemokines after the treatment of cryoablation

274 combined with an anti-IFNAR1 blocking antibody or an isotype control monoclonal antibody (n =

275 5 per group).

276 The statistical significance of differences among multiple groups was determined by one-way

277 ANOVA. *, $P < 0.05$; **, $P < 0.01$. CA, cryoablation; non-CA, non-cryoablation.